CME LIVE OPEN ACCESS

Engineering and Applied Sciences Journal

Review Article ISSN: 3067-8005

DynaMune: An Integrated Ensemble-Based Framework for Comparative Protein Dynamics Using Elastic Network Models

Amirtesh Raghuram*

Department of Biotechnology student at VIT Vellore, India.

Corresponding Author: Amirtesh Raghuram, Department of Biotechnology student at VIT Vellore, India.

Received: 2026 Mar 10 **Accepted:** 2026 Mar 31 **Published:** 2026 Ap 20

Abstract

Normal mode analysis (NMA) and elastic network models (ENMs) provide a rapid and efficient route to probe collective protein motions, but existing tools are fragmented, require heterogeneous parameter choices, and lack a unified framework for ensemble generation, apo–complex comparison, and interface persistence analysis. Here, DynaMune is introduced as an integrated, parameter-aware platform that standardizes ENM/NMA-based dynamics within a reproducible, ensemble-driven workflow. Built on ProDy as its computational backbone, DynaMune automates normal mode and principal component analysis, Gaussian and anisotropic network modeling, perturbation response scanning, domain and hinge decomposition, pocket accessibility profiling, conformational deformation mapping, and systematic quantification of interface contact stability and persistence. An optional immuno informatics extension supports early-stage epitope selection and multi-epitope construct evaluation using dynamics-informed ensemble modeling. The tool was benchmarked on two mechanistically distinct systems: adenylate kinase (ADK), a canonical model of large-scale conformational transitions, and the ACE2–SARS-CoV-2 Spike complex, a structurally constrained protein–protein interface. DynaMune recovered the canonical CORE–LID–NMP transitions, hinge sites, and cracking behavior of ADK, and reproduced the ACE2–Spike interaction hotspot, multimode deformation mechanism, and persistent interfacial contact network reported in crystallographic, cryo-EM, and molecular dynamics studies. These results show that DynaMune reliably captures both intra-protein allostery and ligand-induced interface remodeling. The tool provides a unified, scalable framework for ENM/NMA-based structural dynamics, enabling routine mechanistic interpretation, consistent parameter usage, and publication-ready reporting without external simulations or specialized scripting expertise.

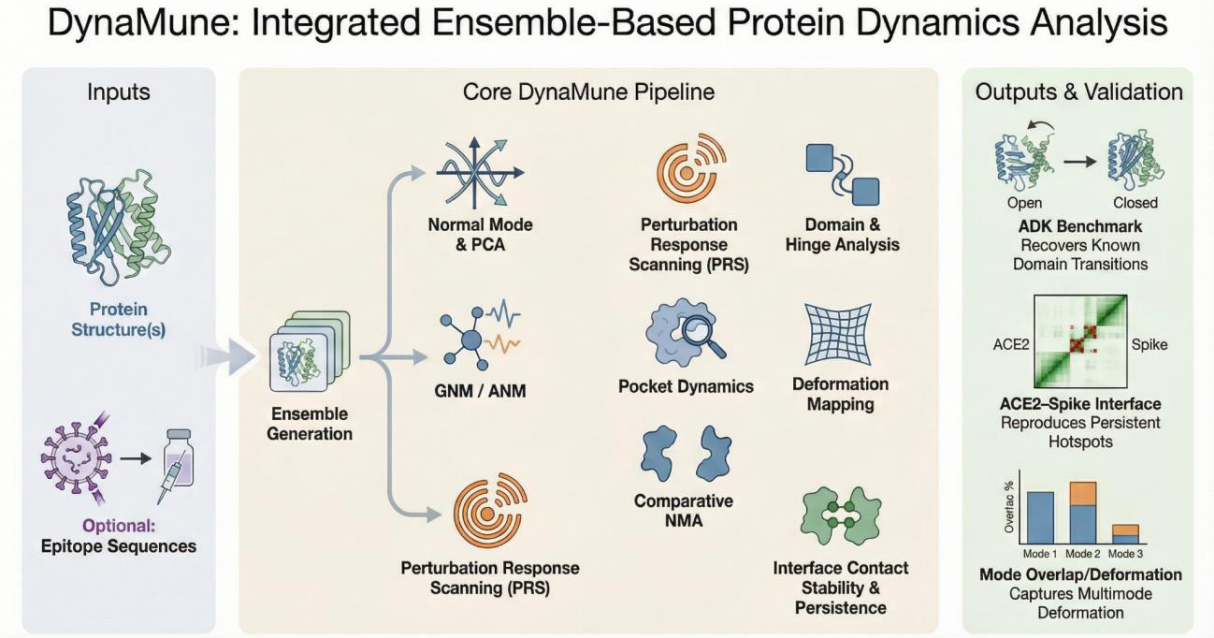

Keywords: Integrated, Framework, Dynamics Analysis, Elastic Network, Molecular Dynamics Studies

1. Introduction

The biological activity of proteins is defined by the dynamic interplay between highly specific structures and the ability to coordinate conformational changes [1,2]. While the tertiary structure supports specificity and stability, it is actually the ability to access and interconvert between alternative sub states (often separated by low energy barriers) that allows for catalysis, allosteric regulation, molecular recognition, and the assembly of complexes [2-4]. For example, transitions in enzyme cycles, ligand-induced regulation, and protein-protein association are physiologically relevant events that result not from a single canonical structure, but from the range of accessible conformations that the protein samples under physiological conditions [4,5]. Recent advancements in structural biology have successfully moved beyond the purely conceptual to experimentally produce the three-dimensional structures of proteins. Improvements in X-ray crystallography and cryo-electron microscopy as well as, more recently, deep learning-based approaches like AlphaFold3, have successfully characterized nearly the entire proteome [6-9]. While these methods provide unique insights, they ultimately generate static snapshots that do not illuminate the range of functionally relevant sub states, nor the pathways of transition between them [4]. Important experimental and computational evidence suggests that many, if not all, biochemical processes such as substrate channeling, domain docking and relay of signals, rely heavily on conformational changes over timescales typically not captured in static structural data [1,5,10].

When function is inferred directly from static structures without considering this dynamic component, there is an inherent risk of functional mis annotation [4,5]. Given that many conformational changes occur at critical regulatory or allosteric sites, and that switching between alternate structural states may be critical for catalysis or signaling events, we cannot assume or predict possible state switching from the starting conformation. This limitation underlies many challenges in drug discovery. That is, the mis annotation of binding sites or drug ability depending on unappreciated conformational dynamics at active or allosteric sites [11,12]. Thus, the gap between static structure and functional understanding remains an important and topical issue in both basic and applied bioscience [1,2].

Molecular dynamics (MD) simulations act as the primary tool for mapping atomistic protein motion, providing key insights into folding, functional switching, substrate binding, and allosteric pathways [1,11]. However, the computational expense and data analysis requirements of MD generally preclude its use for high-throughput annotation, interrogation of large complexes, or rapid exploration of multi-variant structural models, particularly at current proteomic and structural genomics throughput scales. These issues are compounded by the rate at which new models are produced by structural prediction algorithms [13]. Elastic network models (ENMs) and normal mode analysis (NMA) represent an established, efficient theoretical approach to characterizing large-scale, collective motions, which are often fundamental to functionally relevant transitions [14,15]. ENM-NMA models treat proteins as coarse-grained networks, permitting rapid calculation of deformation modes and domain-coupling motions consistent with large conformational changes observed experimentally [14-16]. Benchmark studies have demonstrated that these methods reliably reproduce known motions across a range of systems, including both canonical enzymes and protein assemblies [17,18].

Despite the promise of ENM/NMA for functional analysis, the application of this framework has not been fully realized due to fragmented toolchains, ad hoc parameter selection, and the absence of a consistent and reproducible workflow that analyzes both free and bound (apo/complex) forms [19]. Most pipelines do not have a defined strategy for mapping domain mobility, assessing allosteric sites, and quantifying ensemble contributions at binding interfaces. Existing tools such as DynaMut focus on mutation impact prediction [20]. While DynaMine provides sequence-based dynamics profiles [21]. But neither addresses ensemble-driven conformational sampling or integrated interface dynamics analysis [19,22].

In this paper, we present DynaMune, a fully integrated, parameter-aware software platform designed for the analysis of protein dynamics as derived from ensembles generated with ENM and NMA. DynaMune uses ProDy, a well-established Python package for protein structural dynamics and sequence analysis, as its core computational engine for normal mode analysis, perturbation response scanning, contact network evaluation, and ensemble-based dynamics calculations [23]. Unlike ProDy, which provides modular functionality requiring scripting and manual parameter selection, DynaMune unifies these analyses into an automated, ensemble-driven workflow that standardizes parameter usage, supports direct apo–complex transitions, and produces publication-ready dynamic profiles without requiring external simulations. DynaMune includes functionality for a wide range of analyses, including normal mode and principal component analysis (PCA), perturbation response scanning, domain and hinge analysis, pocket fluctuations, and an explicit approach to study contact persistence and interfacial dynamics all within a unified, reproducible workflow. For proteins of immunological interest, DynaMune provides an optional module enabling early-stage epitope prediction and initial multi-epitope construct evaluation using ENM/NMA-derived ensemble modeling, supporting dynamics-based selection prior to full vaccine design workflows. The approach produces standardized outputs for data analysis with a view toward reproducibility and accelerated comparisons at scale and can use structures that were either experimentally determined or predicted using AI. This integrated capability addresses key methodological gaps, and DynaMune outputs can be directly validated against established structural benchmarks, such as those generated by classical MD [11,16]. iMODS, WEBnm@ and Bio3D are some of the computational frameworks available for ENM/NMA-based dynamics analysis [24-26]. These frameworks offer modular capabilities for tasks

like mode calculation, fluctuation analysis, and coarse-grained modeling. These tools do not, however, offer an integrated workflow that can unify ensemble generation, apo–complex comparison, interface persistence mapping, hinge/domain decomposition, and allosteric evaluation under a consistent parameter architecture. Instead, they function as separate components that necessitate manual scripting, heterogeneous parameter selection, or multi-program coordination. None of these platforms support automated cross-state evaluation (apo → complex) in a single environment, standardize the execution pipeline, or combine outputs into a repeatable format. DynaMune is positioned exactly in this gap.

To validate our approach, we chose two representative systems to assess the scope of the workflow within distinct mechanistic regimes. Adenylate kinase (ADK) is the prototypical model of large-scale domain motions and allosteric transitions and provides a rigorous benchmark for evaluating the platform's intrinsic ensemble accuracy, identification of transition vectors, sensitivity to parameter choices, and recovery of known coupling between mechanical and functional sites [17,27]. In contrast, the human ACE2–SARS-CoV-2 spike complex is a model of a stably docked interface with functionally significant local rearrangement from induced-fit binding [28-30]. This system tests DynaMune's ability to resolve ligand-induced remodeling of an interface, persistent contact mapping, and propagating allosteric during complex formation. In both systems, DynaMune recapitulated published mechanistic pathways and functional benchmarks, identifying functionally relevant dynamic domains, regulatory hotspots, and interface determinants. These findings support the utility of ensemble-based ENM/NMA analysis as a practical, scalable method for robust structural interpretation that incorporates mechanistic information. By making these techniques broadly accessible with reproducible outputs suitable for both experimental and computational research workflows, DynaMune facilitates the next iteration of dynamics-aware annotation in biology, biomedicine, and protein engineering.

2. Methods

2.1. Platform Architecture and Implementation

DynaMune is written in Python and uses ProDy (v2.4+) as the core computational engine for elastic network modeling, normal mode analysis (NMA), perturbation response scanning (PRS), ensemble-based movement sampling, and dynamics-related correlation calculations [23]. The platform has seven modular components which can be executed both individually or in a sequential workflow. The components can be executed through both command line for batch analysis and are also designed for a web-based deployment where users can upload protein structures and perform analyses through the GUI. This dual implementation supports both advanced users and researchers without significant bioinformatics expertise. DynaMune permits the input of structures in PDB format either from experimentally derived (e.g., X-ray or cryo-EM) or computationally predicted (e.g., AlphaFold3 predicted) structures. The user will have the option of providing their own parameters such as cutoff distance, number of modes, ensemble size, etc., at run-time, or allowing these parameters to default to the values that were established through rigorously validated benchmark studies. High-resolution output images (300 dpi PNGs), quantitative data in CSV format, PyMOL script files useful for visual inspection, and structured summaries are provided; this allows for easy integration of output results into an author's manuscript and for downstream use in interpreting results. DynaMune provides support for analyzing both independent structures as well as comparing the results of an analysis performed on the same structure in two different states, i.e., apo and complex.

2.2. Analysis Modules

2.2.1 Normal Mode and PCA Analysis

Normal mode analyses of apo structures are completed through ANM, which allows for calculation of the Hessian matrix for modeling full-length structures while considering only residues within a 15 Å distance from one another (for apo) or a 10 Å distance (if in complex), using the ANM eigenvalues and eigenvectors to identify modes of collective displacements and generating conformational ensembles (10–50 conformers; amplitude controlled by RMSD) through sampling along the dominant modes identified in ANM [14]. Once these ensembles are prepared, PCA is computed to quantify ensemble variance using ProDy's built-in functionality [31,32]. Biologically, this module identifies collective transition pathways and dominant movement patterns associated with functional conformational changes, often reproducing experimentally observed opening/closing transitions and catalytic site reorganization.

2.2.2. Gaussian Network Model (GNM) Analysis

For GNM, the mean-square fluctuations and theoretical B-factor calculations are done using a 10 Å distance cutoff with no directional sampling of ensembles [33]. GNM provides a baseline understanding of the flexibility of the protein. It is primarily useful for identifying regions of structural dynamics in a protein that are susceptible to thermal fluctuations and indicating areas that lead to enhanced conformational adaptability or instability under standard physiological conditions.

2.2.3. Perturbation Response Scanning (PRS)

PRS is performed using the inverted ANM-derived Hessian to quantify how individual residue perturbations propagate through the structure [34]. Residue-wise effectiveness and sensitivity profiles reveal mechanically influential positions and potential relay pathways. This highlights allosteric communication sites and mechanically sensitive residues that govern long-range signal propagation or regulation, often corresponding to experimentally validated control points.

2.2.4. Domain Decomposition and Hinge Identification

Dynamic segmentation of a protein's structural domain is performed through hierarchical clustering of the motion

correlation matrices from the ANM, where those residues that act as hinges are located at the minimum points of fluctuation and at the domain interface [16]. This module provides insight into the mechanical segmentation of a protein, allowing the identification of domains that are rigid bodies, i.e., move as independent entities from each other, and those that are 'hinges', i.e., pivot residues of a flexible domain that dictate the orientation and efficiency of large-scale transitions, such as moving a domain and shifting an interface.

2.2.5. Pocket Dynamics and Accessibility

The pocket regions in the conformational ensemble are evaluated for fluctuations in the volume of the pocket, the root-mean-square deviation of the residues that line the pocket, and accessibility fluctuations [35]. Mechanistic insight into the variability of ligand accommodation based upon these fluctuations will help determine if the pocket acts as a 'rigid' docking or 'induced-fit' site, impacting both the drug ability and binding kinetics of a drug.

2.2.6. Comparative Normal Mode Analysis (Apo vs Complex)

Using independent normal mode calculations on a variety of conformations, this approach allows for comparison of the eigenvectors and ΔRMSFs of these modes [1]. By comparing the results of these calculations against one another, the structural regions that lose their structural rigidity or gain flexibility in response to ligand binding or transition can be defined and provide a mechanism to link flexibility to the stabilization of the energetic transition associated with the motion resulting from ligand binding [36].

2.2.7. Conformational Deformation Mapping

The transition from one conformational state to another is presented in terms of the intrinsic ANM modes of the aligned structures [27]. Analysis of the mode overlap, and mode-specific overlap cumulatively identifies how similar the intrinsic dynamics are to the biological transition. This provides an indication of whether the functional motions that occur will be driven by the energetically favorable deformation of the native state or if they will need to be stabilized externally, thus providing an understanding of how the encoded intrinsic motions drive the transition of conformational states [37].

2.2.8. Interface Contact Stability and Persistence

The persistence and stability of contact interfaces between different chains or domains are assessed via an ensemble of conformations using a 4.5 Å cut-off (6 Å for permissive screening) [38]. Interaction frequency and persistence scores are generated, with network relationships developed. This data provides a biological perspective of where the interface hotspots (dynamically stable) are in relation to where all residues of the protein are likely to be participating in the formation of a protein complex [39].

2.2.9. Default Parameters Used Across Modules

The default parameters used across all the modules are listed in Table 1.

Module / Submodule	Parameter	Default value (used by DynaMune)	Reference / Note
ANM	interaction cutoff	15 Å	ProDy defaults / implementation. [23]
	modes computed	20 (first non-zero modes)	ProDy manual / common practice.
GNM	interaction cutoff	10 Å	ProDy defaults / literature.
PRS (Perturbation Response Scanning)	perturbation magnitude	1.0 Å (perturbation amplitude)	Standard PRS implementation; see NMA/allostery reviews. [1]
Conformer generation	ensemble size	10 conformers (default)	ProDy-based ensemble sampling; configurable by user.
	sampling amplitude / RMSD target	~0.8–1.5 Å (physiological range)	Set in pipeline to avoid non-physical distortions.
Deformation analysis	projection modes	first 20 ANM modes	
Contact detection	heavy-atom residue–residue cutoff (general contact)	5.0 Å (per-residue heavy-atom)	
Contact detection — H-bonds	donor–acceptor cutoff	3.5 Å	[40]
Contact detection — Salt bridges	O–N cutoff	4.0 Å	Commonly used cutoff in structural studies (see review literature). [41]
Contact detection — π–π (aromatic)	centroid–centroid / ring distance	7.0 Å	[42]

Contact detection — Cation–π	distance cutoff	6.0 Å	[42]
Contact detection — Hydrophobic	heavy-atom cutoff	5.0 Å	[43]
Contact detection — Disulfide	S–S distance	2.5 Å	[44]
SASA / surface analysis	probe radius	1.4 Å (Shrake–Rupley)	[45]
Output / reporting	persistence thresholds	stable ≥ 75% (high), moderate ≥ 50%, transient < 25%	Chosen for interpretability; configurable by user.
General defaults	file formats / outputs	CSVs, PNGs, JSON summary	standardized for publication-ready output.

Table 1: Default Parameter Settings for All Dynamune Modules

2.3. Execution Workflow and Output Standardization

An execution pipeline is standardized for each of the modules being analysed. Users define the parameters for use in each of the modules. During the default execution, 20 modes will be used together with ensemble sampling using 10 different conformers, with one or more of the conations being maintained within the physiological limits of displacement (generally 0.8–1.5 Å). Therefore, all outputs are prepared for publication and/or review by consolidating numerical tables representing output data, graphical outputs of the contact interfaces and/or graphical output scripts. The execution of the software will occur through either the use of command-line scripts for batch operations and/or from the server for remote interaction with the end user; therefore, it has a capability for large-scale application both for the purpose of academic research and education/training purposes.

2.4. System Requirements and Implementation Details

DynaMune is implemented in Python 3.10 and uses ProDy as its core computational engine for ENM/NMA calculations. All modules can be executed through a command-line interface for batch workflows or through a Flask-based web interface for interactive use. The platform is fully cross-platform and requires only standard scientific Python libraries, making it deployable on personal workstations or shared computing environments.

2.5. Computational Performance

The workflow is designed for lightweight execution and does not require GPU or MD-level hardware. On a standard laptop-class CPU (4–8 cores), complete ANM/GNM ensemble generation, deformation analysis, contact mapping, and persistence evaluation typically complete in under 3–5 minutes for proteins up to ~800 residues. Even multi-module runs remain within a few minutes, demonstrating that the methodology is practical for large-scale comparative studies and routine structural analysis (Figure 1).

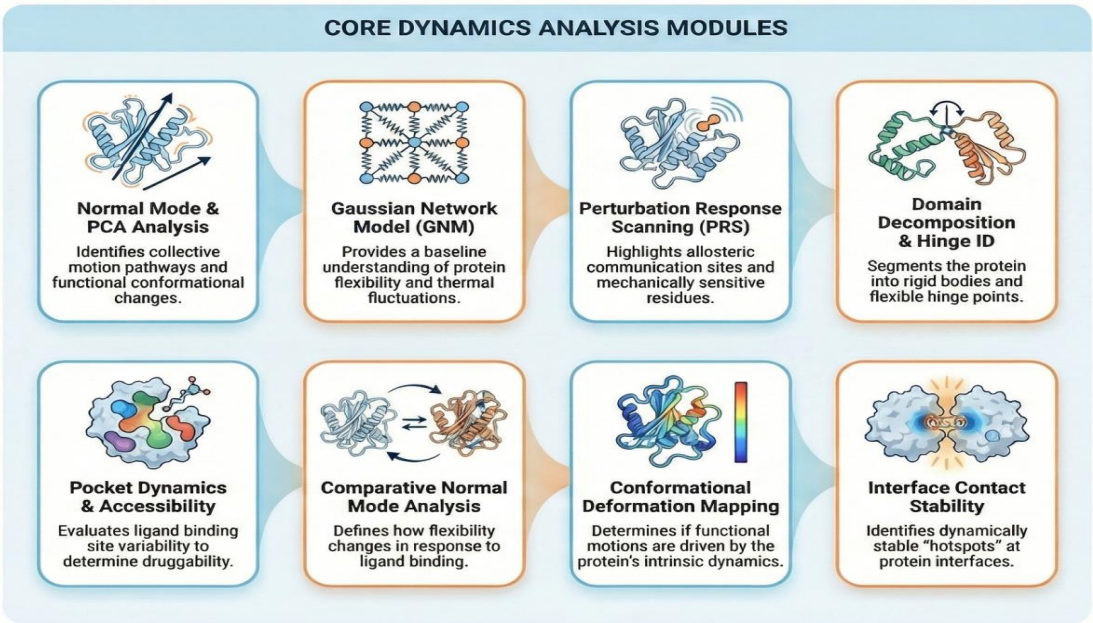

Figure 1: Dynamune Core Dynamics Analysis Workflow. Overview of Input Processing Prody-Based Computational Execution, and Eight Analytical Modules (Normal Mode/Pca, Gnm, Prs, Domain–Hinge Detection, Pocket Dynamics, Comparative Analysis, Conformational Deformation Mapping, and Interface Contact Persistence), Converging into Standardized Structural and Quantitative Outputs.

2.6. Optional Dynamics-Assisted Immunoinformatic Module

This module supports preliminary construct evaluation and is not intended to replace dedicated immunoinformatic platforms for clinical vaccine development (e.g., IEDB, Vaxign, or full immune simulation pipelines). DynaMune includes an optional module for preliminary immunogen screening that supports early-stage multi-epitope vaccine construct design with subsequent structural dynamics evaluation.

2.6.1. Epitope Prediction and Safety Filtering

Linear B-cell epitope prediction is performed using NetBCE (executed in an isolated Python 3.7 environment) [40-46]. Cytotoxic T lymphocyte (CTL) and helper T lymphocyte (HTL) epitopes are predicted via API access to NetMHCpan-4.1 and NetMHCIIpan-4.1, respectively, with user-defined HLA allele selection [47]. Toxicity screening is conducted using ToxinPred3, and allergenicity assessment using AlgPred 2.0. Unsafe sequences can be excluded prior to construct assembly [48,49].

2.6.2. Construct Design

Selected epitopes are organized into multi-epitope constructs using user-specified adjuvants (e.g., β-defensin, PADRE, CTB, 50S ribosomal protein, RS09, HBHA, HABA) positioned at the N-terminus using an EAAAK linker. Six predefined arrangement templates allow rotational ordering of CTL, HTL, and B-cell epitopes with configurable linkers (AAY, GPGPG, KK, or EAAAK) between segments.

2.6.3. Physicochemical Characterization and Dynamics Evaluation

Physicochemical profiling (molecular weight, hydropathicity, instability index, theoretical pI, aliphatic index) is calculated using the Port Param implementation within Bio Python [50]. Tertiary structure prediction of the full fusion protein is performed via API access to ESMFold [51]. The predicted model is directly passed to ProDy for ANM- or GNM-based analysis using the same default cutoff and mode parameters as for standard structures, enabling estimation of flexibility, potential hinge positioning, and ensemble-based conformational stability. This integration supports dynamics-aware prioritization of candidate vaccine constructs prior to refinement in dedicated immunoinformatic pipelines (Figure 2).

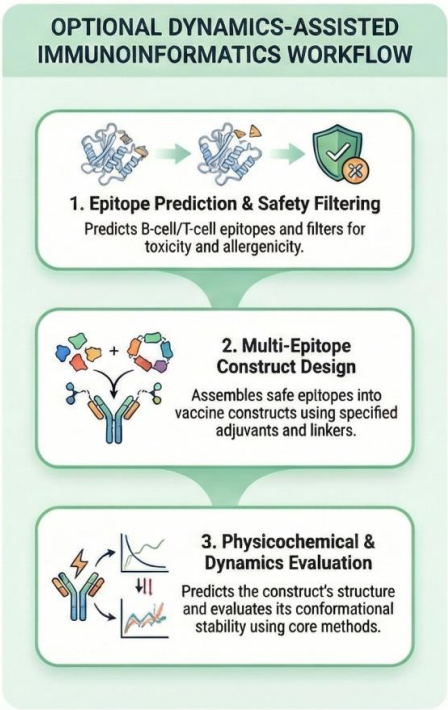

Figure 2: Dynamics-Assisted Immunoinformatic Workflow. Sequential Pipeline from Epitope Prediction Through Safety Filtering, Construct Design, Physicochemical Analysis, Structure Prediction, and Dynamics Validation. Outputs Inform Downstream Vaccine Development Pipelines (e.g., IEDB, Vaxign).

2.7. Software Dependencies and Availability

DynaMune requires Python 3.8 or newer (with NetBCE epitope prediction requiring Python 3.7 in an isolated environment), ProDy ≥2.4, and standard scientific computing libraries including NumPy, SciPy, Matplotlib, Seaborn, and Bio Python. The immunoinformatic module integrates external prediction services accessed via API: ESMFold for tertiary structure prediction (via ESMFold API), NetMHCpan-4.1 and NetMHCIIpan-4.1 for MHC binding predictions (via IEDB Nextgen tools). ToxinPred3, AlgPred2.0, and NetBCE require local installation. API-dependent modules require active internet connectivity and are subject to the respective service availability and usage policies. The platform is fully script-executable and supports deployment in local research environments as well as web-based execution.

3. Validation and Case Studies

3.1. Mechanistic Benchmarking Using Adenylate Kinase (ADK)

3.1.1. System Preparation

Adenylate kinase was selected as a benchmark system using its closed (PDB ID: 1AKE) and open (PDB ID: 4AKE) conformational states [17,52,53]. Structures were manually cleaned in PyMOL to remove solvent and heteroatoms [54]. No structural refinement was applied, as both entries were complete and suitable for direct analysis.

3.1.2. Normal Mode Execution Setting

The parameters for normal mode calculations were chosen according to structural conformation. For the closed state (1AKE), ANM was executed using a 20 Å interaction cutoff with default γ = 1.0 to account for extended elastic coupling characteristic of its restricted conformation [55]. GNM calculations for the same state were performed using a 10 Å cutoff [33]. For the open state (4AKE), ANM was run using a 15 Å cutoff with default gamma scaling (γ = 1.0), while GNM again used a 10 Å cutoff. Twenty non-zero modes were used for all analyses, and ten ensemble conformers were generated per structure.

3.1.3. ANM-Derived Mechanistic Interpretation

ANM analysis reproduced the canonical conformational transition previously described for adenylate kinase. In the closed state (1AKE), the dominant low-frequency modes indicated motion originating within the CORE and propagating toward the LID and AMP-binding domains, consistent with the direction of substrate-induced opening reported previously [52, 56-58]. Limited fluctuation amplitudes and narrow conformer clustering reflected restricted mobility, supporting its kinetically stabilized configuration (Figure 3).

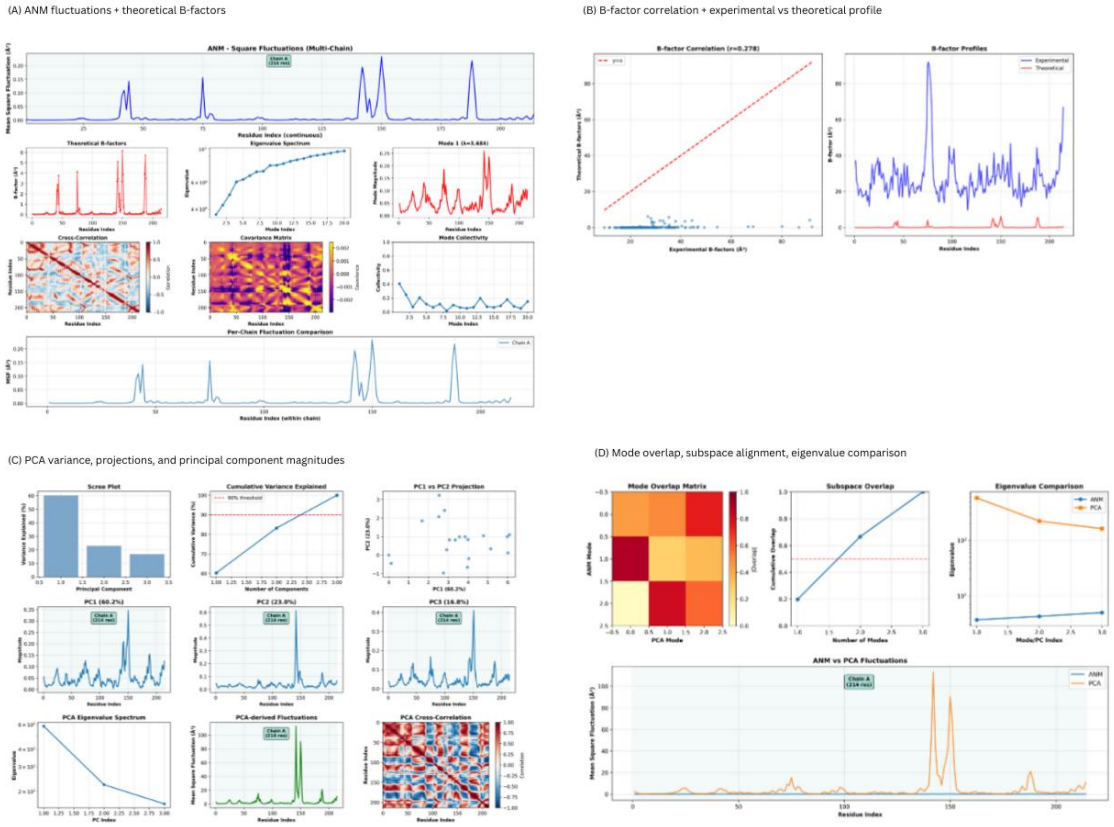

Figure 3: ANM and PCA-Based Ensemble Dynamics Analysis of The Closed Conformation (1AKE). (A) ANM-Derived Fluctuations and Theoretical B-Factor Estimation. (B) Comparison of Theoretical and Experimental B-Factors (Pearson Correlation r = 0.28). (C) PCA Trajectory Distribution, Variance Explanation, and Component Representation. (D) Mode Overlap and Subspace Convergence Between Anm and Pca, Confirming Intrinsic Alignment with Functional Transition Direction.

Conversely, the open state (4AKE) exhibited broader displacement distribution and increased fluctuation at substrate-access regions, indicative of a relaxed transition-ready topology. Mode–PCA overlap was high for both conformations, with near-complete alignment when including the first three modes, validating that intrinsic ANM-derived motions capture the experimentally observed pathway (Figure 4). Theoretical B-factor correlation improved from 0.28 (closed) to 0.78 (open), matching observations that the open state accommodates greater localized flexibility [52,59]. These results confirm that DynaMune's ANM ensemble resolves state-dependent transition mechanics coherently with literature models, successfully capturing both the restricted pre-transition posture and the permissive active conformation.

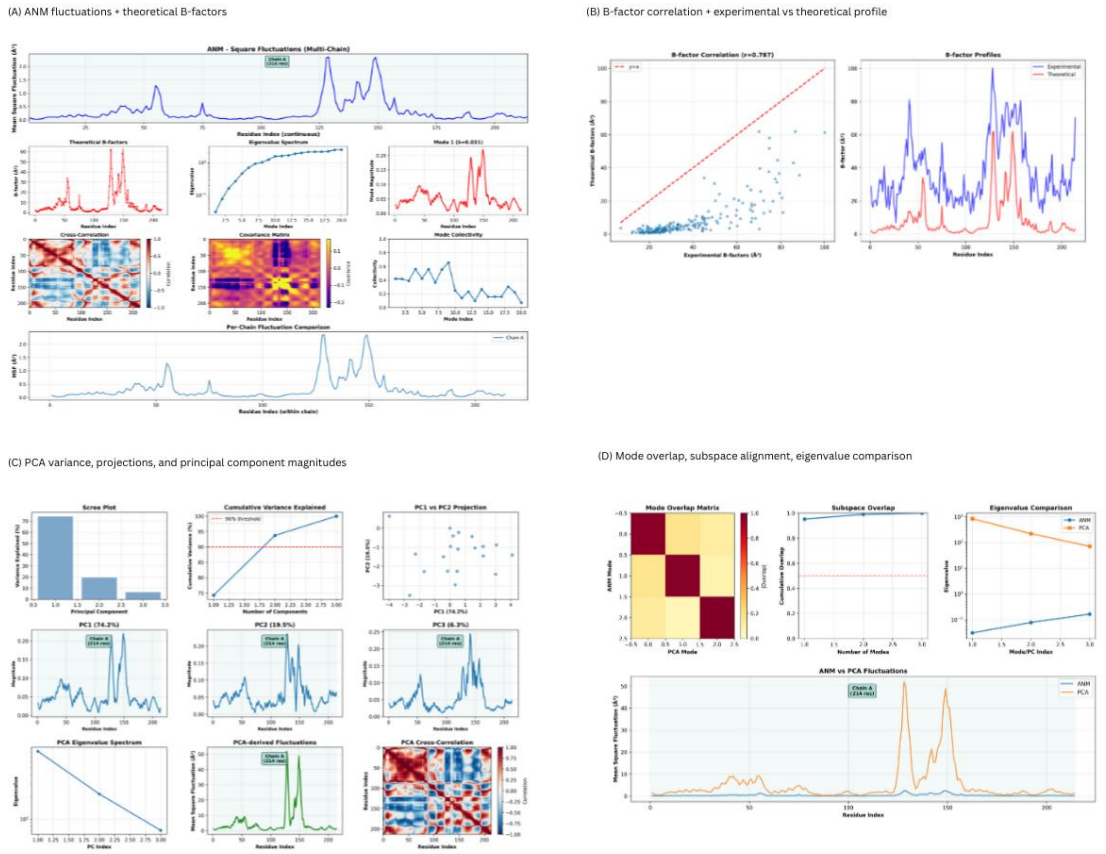

Figure 4: ANM and PCA-Based Ensemble Dynamics Analysis of The Open Conformation (4AKE). (A) ANM-Derived Fluctuations and Theoretical B-Factor Estimation. (B) Comparison of Theoretical and Experimental B-Factors (Pearson Correlation r = 0.78). (C) PCA Trajectory Distribution, Variance Explanation, and Component Representation. (D) Mode Overlap and Subspace Convergence Between ANM and PCA, Confirming Intrinsic Alignment with Functional Transition Direction.

3.1.4. GNM-derived Flexibility Assessment

GNM captured fluctuation amplitudes but did not resolve directional domain coupling or hinge behavior in either conformation, consistent with its isotropic formulation[55,59]. In the closed state (1AKE), theoretical B-factor correlation improved to r = 0.51 compared to ANM, but localized mobility, particularly around the LID domain, remained underestimated relative to experimental reports (Figure 5) [56]. Mode collectivity and eigenvalue distribution indicated restricted fluctuations without coherent transition direction [15].

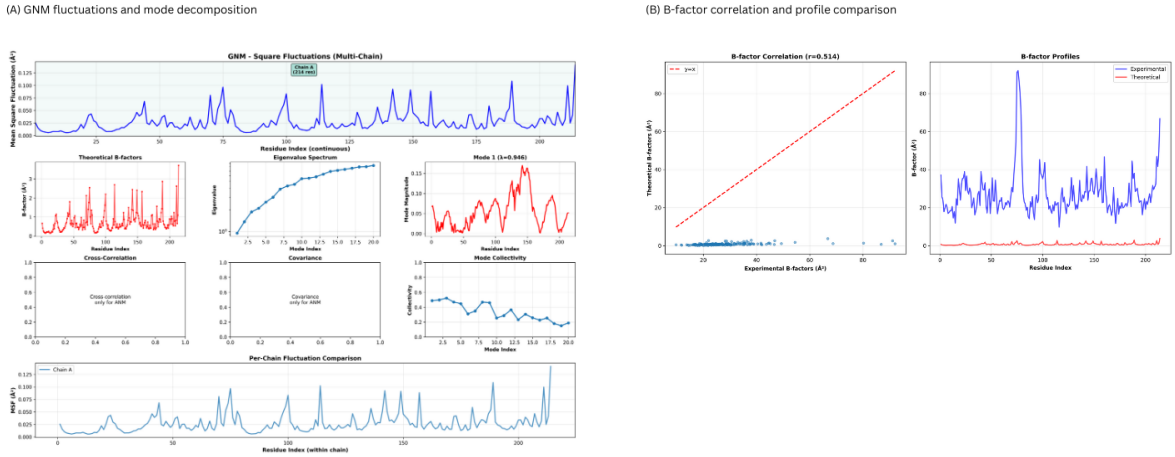

Figure 5: GNM-Derived Flexibility Assessment of The Closed Conformation (1AKE). (A) GNM Square Fluctuations, Theoretical B-Factors, Eigenvalue Spectrum, Mode Shape, Mode Collectivity, Cross-Correlation (ANM Only), Covariance (ANM Only), and Per-Chain Fluctuation Comparison. (B) Theoretical vs. Experimental B-Factor Comparison (r = 0.51) with Profile Overlay.

The open conformation (4AKE) showed increased flexibility in substrate-access regions, with r = 0.80 indicating better agreement with experimental dynamics (Figure 6). However, the absence of rotational coupling and cooperative displacement limits mechanistic interpretation, which was captured by ANM [55]. GNM provides reliable state-dependent fluctuation magnitudes but lacks the capacity to infer functional transition mechanics, which required ANM-based directional analysis [55].

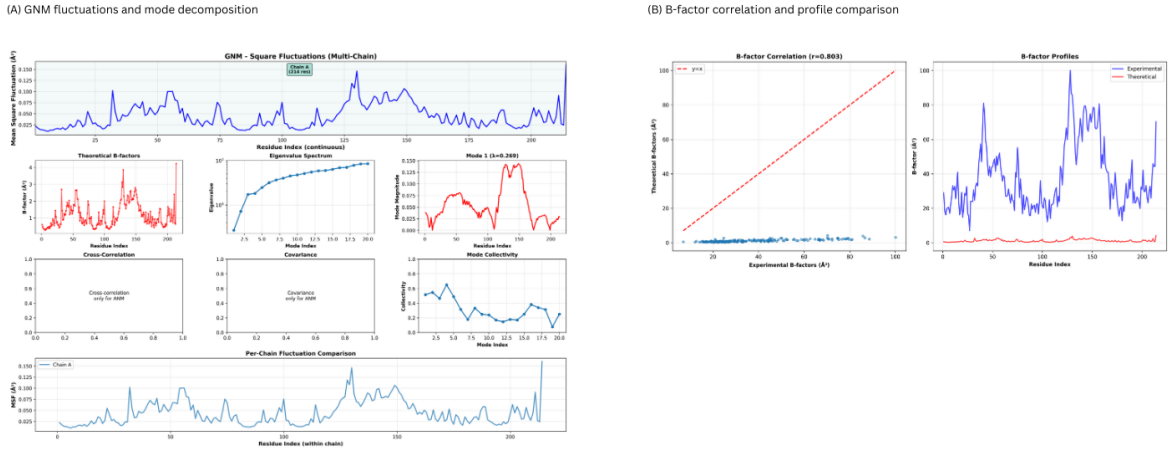

Figure 6: GNM-Derived Flexibility Assessment of the Open Conformation (4AKE). (A) GNM Square Fluctuations, Theoretical B-Factors, Eigenvalue Spectrum, Mode Shape, Mode Collectivity, Cross-Correlation (Anm Only), Covariance (Anm Only), And Per-Chain Fluctuation Comparison. (B) Theoretical vs. Experimental B-factor Comparison (r = 0.80) With Profile Overlay.

3.1.5. Perturbation Response Scanning (Prs)-Based Allosteric Control

Analyzing the closed conformation (1AKE) via perturbation response scanning (PRS) showed that significant perturbation response efficiency was associated with the CORE N-terminal (ILE4–LEU6) and hinge (LEU83–PHE86) regions of the LID, indicating that those areas have the capacity for conformational displacement. In addition, several high hub scores were identified at residues 29–32 and 80–82, indicating these locations represent the inter-domain stabilization interface typical of the closed state [57]. The sensitivity peaks in the AMP-binding domains (residues 142–150, 187–189) remained highly confined during all perturbations, indicating that inter-domain signal transmission is restricted primarily to the catalytic core with little or no significant impact on opening [17]. Therefore, the PRS matrix demonstrated a mainly diagonal-based perturbation response pattern, indicating that localized perturbations are primarily restricted, thus limiting the communication across the domains and preventing any large-scale transition (Figure 7) [60,56].

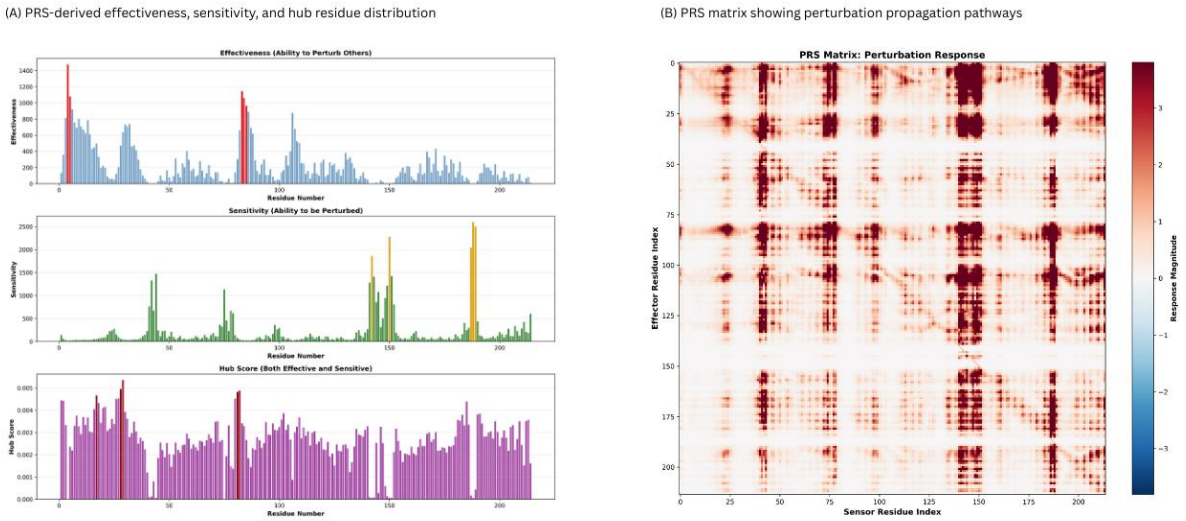

Figure 7: PRS-Based Allosteric Control Analysis of The Closed Conformation (1AKE). (A) PRS-Derived Effectiveness, Sensitivity, and Hub Residue Distributions. (B) Perturbation Response Propagation Matrix Illustrating Predominantly Localized Response Patterns.

In the open conformation (4AKE), perturbation response efficiency was maintained primarily in the catalytic regulatory core region (ILE4–LEU6, PHE86) [57]. However, the peripheral residues, including TYR182 and LEU107, exhibited increased perturbation response efficiency as a result of increased inter-domain signalling after relaxation [56]. Sensitivity distributions shifted toward residues 127–152. This indicates greater potential for responding in the substrate-access region. Residue sensitivity has also shifted to SER30–THR31 (LID) [57]. This change in sensitivity reorganized the residue interaction network into the more dynamic transition-attainable state (Figure 8) [52]. The data presented in the PRS heatmap indicated that there was more long-distance propagation in the open state compared to the closed state [60]. This correlates with a more permissive arrangement of the molecule [52].

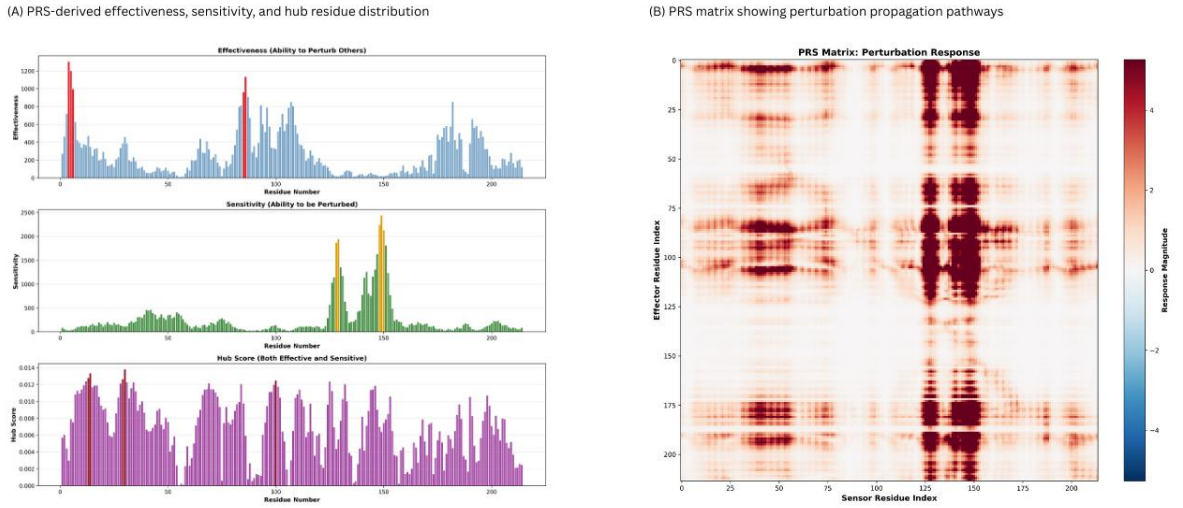

Figure 8: PRS-Based Allosteric Control Analysis of The Open Conformation (4AKE). (A) PRS-Derived Effectiveness, Sensitivity, and Hub Residue Distributions. (B) Perturbation Response Propagation Matrix Demonstrating Enhanced Long-Range Communication.

The data summarized above indicate that, overall, distinct regimes of dynamic control were present across the global conformational states. The closed state retains kinetic restrictions due to localized stabilization and limited allosteric propagation [56].In contrast, the open state exhibits more redistribution of control nodes and greater distal responsiveness [52]. Finally, as demonstrated by DynaMune's ability to map state-specific regulatory mechanisms of signaling activity, it is able to capture the basis for allosteric communication and facilitate dynamic interactions between different conformations [60].

3.1.6. Pocket Dynamics Analysis

The closed conformation (1AKE) has a structurally confined pocket with RMSF values that tend to remain below the overall mean of the ensemble of structures calculated for this pocket area with only a few residues (approximately residues 40–45 and 140–145) localized around the active site showing higher RMSF values [52]. Therefore, these two localized areas have minimal flexibility but represent breathing regions rather than domains that move away from substrate confinement [56]. Residues 40–45 (based on current structural mapping) overlap with the phosphate-binding region, while residues 140–145 align with the adenine-recognition site observed in AMP-bound structural studies of adenylate kinase, indicating that the detected fluctuations occur within ligand-positioning segments rather than transition-driving regions [17]. Fluctuation mapping of the distance from the catalytic core identifies shape variance occurring mainly within clusters of residues and shows no consistently distributed patterns, indicating that the pocket is rigid and catalytically restricted and cannot easily reorient due to the limited flexibility in the pocket geometry [52]. The pocket volume fluctuation calculations, showing small values centered around the mean, indicate that the pocket samples only narrow ranges of conformations, suggesting the pocket remains locked in its conformation (Figure 9) [58].

Figure 9: Pocket Dynamics Analysis of The Closed Conformation (1AKE). (A) Residue Flexibility (RMSF) and Pocket Shape Variance Based on Inter-Residue Distance Fluctuations. (B) Pocket Volume Dynamics Over Conformer Ensemble and Corresponding Volume Distribution

In contrast, the open conformation (4AKE) exhibits higher RMSF values for the regions surrounding the substrate access areas and the hinge-interacting residues, facilitating substrate accommodation during the transition state [56]. In the open form, hinge-associated residues contribute to structurally adaptive volume expansion, reducing the energetic barrier necessary for catalytic transition, which is consistent with previously described cracking-dependent motion [56]. Shape variance plots for each of the residue clusters demonstrate a much wider distribution of the shape fluctuations, which reflects that the open catalytic site has greater flexibility potential and the ability to access more conformational states than the closed state [52]. The open conformation shows wider sample ranges and broader variability across conformer indices than the closed conformation (Figure 10) [58]. These findings suggest that, while the open catalytic site allows for the redistribution of local flexibility to permit substrate engagement, the closed form represents the sterically restricted active site conation that provides maximum stabilization and minimal potential for displacement [17].

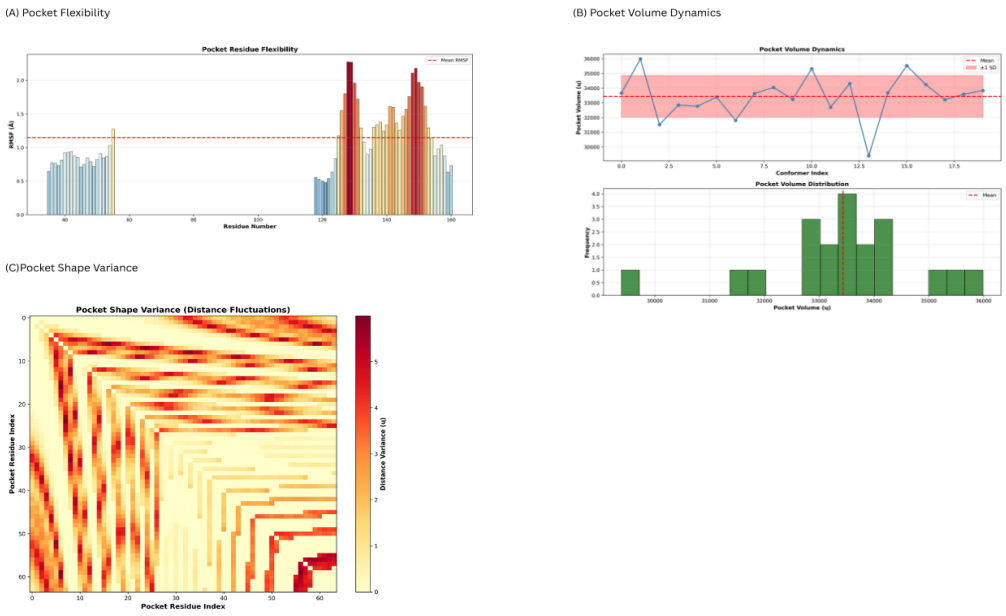

Figure 10: Pocket Dynamics Analysis of The Open Conformation (4AKE). (A) Residue Flexibility (RMSF) and Pocket Shape Variance Based on Inter-Residue Distance Fluctuations. (B) Pocket Volume Dynamics Over Conformer Ensemble and Corresponding Volume Distribution

3.1.7. Domain Hinge Analysis

The closed conformation (1AKE) demonstrated a highly segmented domain organization (18 domains), each with defined localized motion boundaries with little to no domain cooperation across all 18 domains. Cross-correlation analysis showed strong intradomain positive correlation and predominantly anti-correlated or weak interdomain interaction across all 18 domains, consistent with kinetically restricted architecture [52]. Thus, motion propagation occurs within a locally defined structural segment, suggesting that strongly linked residues are not globally coupled as a whole. Hinge analysis showed that high-scoring residues cluster around known interdomain transition regions, specifically residues 90–95, 32–36, and 105, which facilitate conformational transitions. These residues are associated with structural input required to produce conformational changes when moving from closed to open form and supported by computational model results that show they are located exactly at the boundaries of all 18 domains. The stiffness profile indicates that high-stiffness regions (relatively compliant by design) surround residues segregated from the rest of the structure and support that transitional motion from closed to open forms depends on very localized crack-like modes of motion; extensive flexibility is present only at the very core of the structural backbone of the closed conformation (Figure 11) [56].

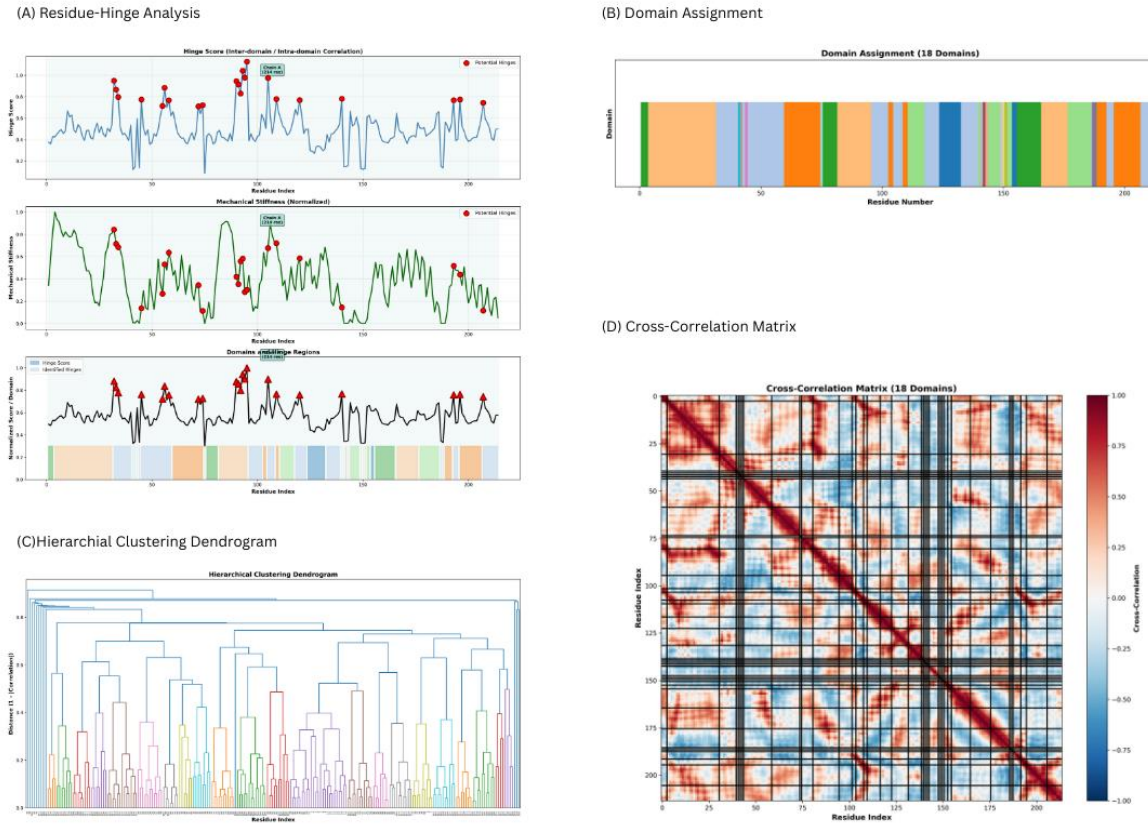

Figure 11: Domain Decomposition and Hinge Analysis of The Closed Conformation (1AKE). (A) Hinge Score Distribution Across Three Conformational States (Inter-Domain Correlation, Intra-Domain Correlation, and Mechanical Stiffness). (B) Domain Assignment Showing 18 Dynamic Domains with Distinct Motion Boundaries. (C) Hierarchical Clustering Dendrogram Illustrating Domain Grouping Based on Correlated Motion. (D) Cross-Correlation Matrix with Domain Boundaries Overlaid (Black Grid Lines), Demonstrating Strong Intradomain Correlation (Red Blocks Along Diagonal) and Weak/Anti-Correlated Interdomain Interactions (Blue Off-Diagonal Regions)

In contrast, the open conformation (4AKE) displays fewer dynamic domains (6 domains) that are comprised of larger spans of residues than that of closed conformation, which demonstrates a transition away from fragmented motion domains into more integrated motion modules. As such, the cross-correlation matrix for the open conformation indicates more extensive areas of positive cooperative correlation, which suggests a greater degree of uniformity in the pattern of movement of the open conformation, consistent with a more permissive topology [52]. The hinge residues of the open conformation were found to be more widely distributed across interdomain interfaces than were the hinge residues of the closed conformation; in particular, the residues LEU5, 139–145, and 213–214 demonstrate the relationship of hinge residues to increased overall flexibility due to the presence of larger mechanical domains. These residues correspond to sites described as modulating the ability of enzymes to expand their conformation and access substrates and therefore confirm aspects of the mechanism of transition to the cracked state in adenylate kinase (Figure

12) [56]. Moreover, the hinge regions of the open form are embedded within larger mechanically permissive domains; thus, they support the concept that hinge regions are crucial for the establishment of dynamic pathways of rearrangement.

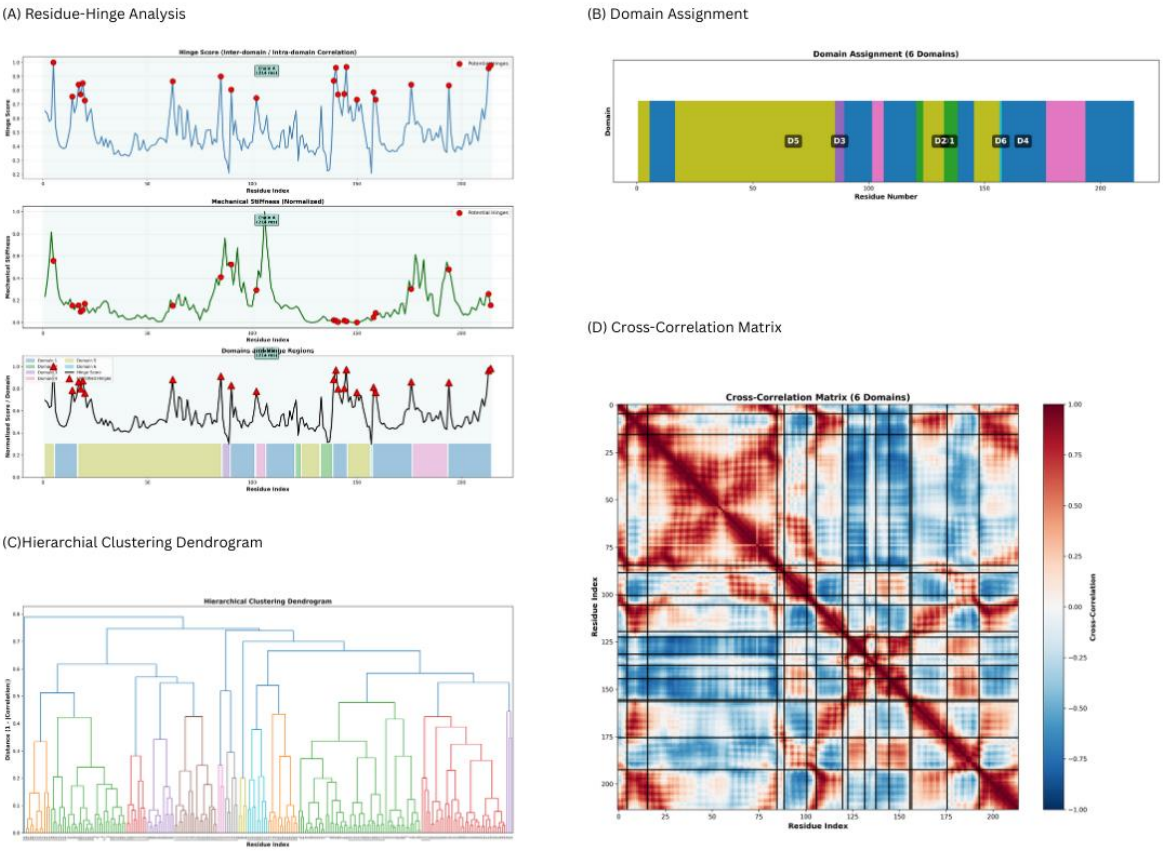

Figure 12: Domain Decomposition and Hinge Analysis of The Open Conformation (4AKE). (A) Hinge Score Distribution Across Three Conformational States (inter-domain correlation, intra-domain correlation, and mechanical stiffness). (B) Domain Assignment Showing 6 Dynamic Domains with Distinct Motion Boundaries. (C) Hierarchical Clustering Dendrogram Illustrating Domain Grouping Based on Correlated Motion. (D) Cross-Correlation Matrix with Domain Boundaries Overlaid (Black Grid Lines), Demonstrating Extended Regions of Positive Cooperative Correlation (Red Blocks Along Diagonal And off-Diagonal) Indicating Enhanced Global Coupling And Unified Movement Across Domains.

The combined results indicate that closed conformation is subjected to kinetic restriction by highly fragmented domain segmentation due to strictly localized mechanics of the hinge residues, while open conformation employs less fragmentation of the resultant domains, which are substantially larger in size than the corresponding domains of closed conformation and includes hinge residues that are optimally positioned to provide for greater coordinated flexibility and adaptability of the conformation [52,56].

3.1.8 Apo-State Mechanistic Integration

Utilizing the analysis methods of ANM, GNM, PRS, pocket dynamics, and domain hinge decomposition, we observed that the closed conformation has a kinetically locked structure with high segmentation, limited fluctuation, and localized displacement due to cracking in the hinge residue regions [56]. The closed conformation also shows a narrow range of variability when approaching the energy transition from closed to open. In contrast, the open conformation displays readiness for transition, characterized by fewer contiguous domains, hinge residues dispersed over broader mechanically permissive regions, greater fluctuation magnitude, and a much wider range of pocket conformations along the transition pathway [52]. This suggests that when the closed conformation transforms to open, the topology is already primed for substrate placement. Examining energetic changes during the conformational shift indicates that adenylate kinase transitions from closed to open not by gradual relaxation, but via localized hinge activation that overcomes kinetic locks, followed by a concerted reorientation of domains [56]. DynaMune accurately distinguishes these mechanisms by identifying the pre-transition rigid state of the closed conformation and capturing the dynamic features of the open conformation.

3.2. Ligand-Induced Modulation of Conformational Dynamics in The Ace2–Spike Complex

3.2.1. System Preparation

The human ACE2 ectodomain was analyzed in its apo state using chain A of PDB ID 1R42 (native ACE2) and in its ligand-bound state using the ACE2–SARS-CoV-2 spike receptor-binding domain complex from PDB ID 6M0J [28,61]. Both

the structures were processed using the same workflow which was applied for the ADK systems (see Methods, Section 3.1.1). The DynaMune workflow was executed with identical ensemble generation and normal mode parameters to enable a direct comparison between intrinsic (apo) and ligand-induced (complex) dynamic modulation.

3.2.2. ANM-Based Conformational Comparisons

Recent research aligns with earlier findings showing that ACE2 does not simply undergo ligand-induced rigidification when it is engaged by the Spike protein of SARS-CoV-2; however, cryo-electron microscopy and normal mode analysis show that upon binding, ACE2 undergoes a redistribution of dynamical modes rather than simply having its vibrational modes damped [62]. The low diagonal overlap of 0.015 and the moderate best-match alignment with a mean of 0.316 indicate that the intrinsic apo vibrational patterns of ACE2 have been significantly overwritten and that the motion of ACE2 vibrational modes has been selectively reallocated into functionally redirected vibrational modes [63]. The modes that remain most similar (modes 5 and 10; 0.551 and 0.546 respectively) correspond to regions that have previously been implicated in allosteric communication between the binding interface and more distal enzymatic regions of ACE2 [63]. Additionally, the ΔRMSF profile that indicates local stabilization at the binding interface of ACE2 while supporting distal redistribution of flexibility mirrors the dynamic adaptability previously demonstrated in ligand-modulated studies of ACE2; the binding of ligands to ACE2 appears to cause a shift to a more primed, mechanically recalibrated structure rather than just compressing it (Figure .13) [64,65].

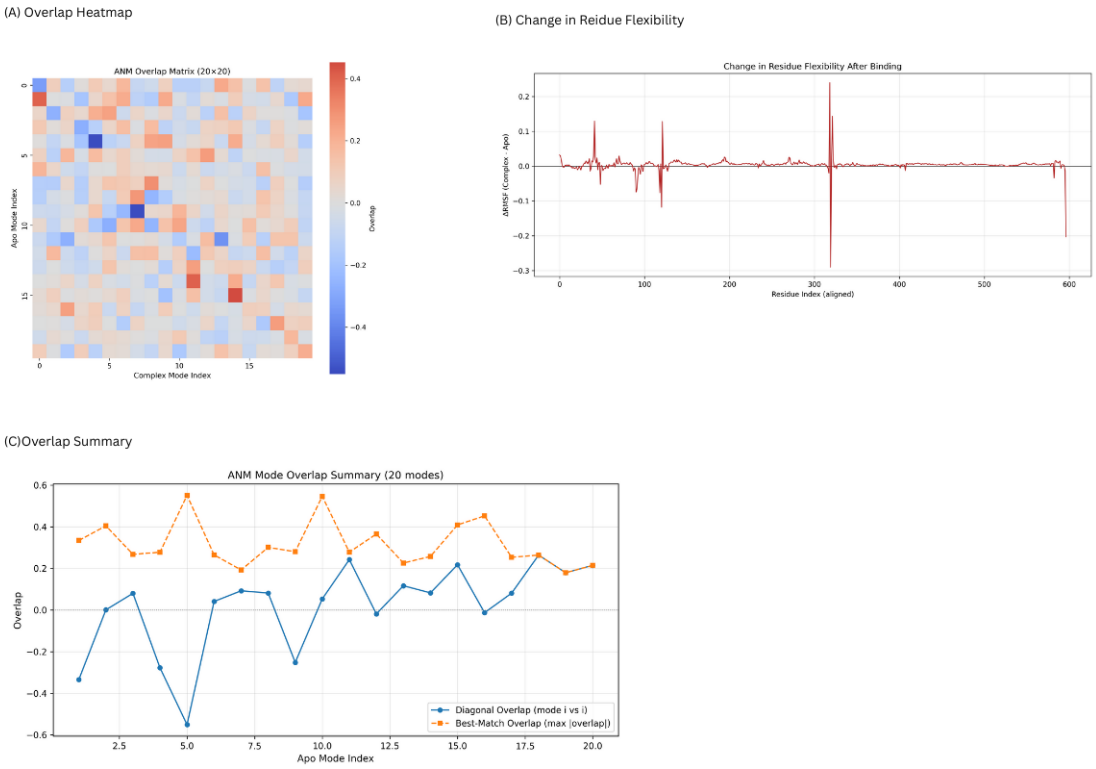

Figure 13: ANM-Based Conformational Comparison Between Apo and Spike-Bound ACE2. (A) ANM Overlap Matrix (20×20 Modes) Showing Low Diagonal Overlap (0.015) and Scattered Patterns, Indicating Mode Redistribution Upon Binding. (B) Change in Residue Flexibility (ΔRMSF) Showing Stabilization at The Binding Interface (~Residues 300-350) with Distal Flexibility Redistribution. (C) Mode Overlap Summary Comparing Diagonal (blue) and best-match (orange) overlap. Low Diagonal and Moderate Best-Match Values (Mean = 0.316) Confirm Selective Mode Reallocation Rather Than Dampening, with Modes 5 And 10 Retaining Highest Similarity (0.551, 0.546)

Therefore, the current results are consistent with prior findings suggesting that ligand interactions with ACE2 provide long-range elastic adjustments rather than a fixed immobile structure; thus, there is clear support for the concept of a mechanically driven receptor remodeling process rather than a lock-and-key mechanism [66]. These findings refine current structural models by indicating that Spike binding does not stabilize ACE2 into a restricted binding conformation but instead actively promotes a mechanically pre-arranged, transition-ready con Figure duration via selective repurposing of internal motion modes—a process consistent with allosteric-driven engagement rather than passive stabilization [62,63].

3.2.3. Deformation Analysis

To analyse the impact of Spike binding on ACE2 dynamics, the conformational deformation vector between the apo (1R42) and Spike-bound (6M0J) states was mapped onto the apo ANM modes. The squared overlaps showed that no one mode was responsible for the deformation caused by binding.

Modes 6 and 20 showed the largest individual squared overlaps (0.13 and 0.10, respectively), each contributing approximately 13% and 10% to the total deformation. Secondary contributions came from modes 2, 10, 12, and 14 (squared overlaps 0.02–0.03 each, representing 2–3% contribution). Notably, even the top-contributing mode accounted for only ~13% of the total deformation, and all individual mode overlaps remained well below the 50% threshold. This distributed pattern indicates that the Spike-induced conformational shift is not encoded along a single pre-existing soft mode but is instead assembled from multiple global and mid-frequency motions.

This behavior is in line with earlier simulations that demonstrate that, instead of merely moving along a native dominant mode, Spike binding perturbs ACE2 structural ensembles by reweighting motion subspaces [65-69]. Instead of freezing the receptor into a rigid complex, Spike engagement modifies correlations between the peptidase and neck domains and redistributes ACE2's collective motions, according to normal mode and MD analyses [70]. The multi-mode requirement observed here supports that picture: binding appears to recruit and recombine several intrinsic motions into a new, Spike-stabilized deformation pathway rather than following a single, ligand-preured trajectory (Figure 14) [68-72].

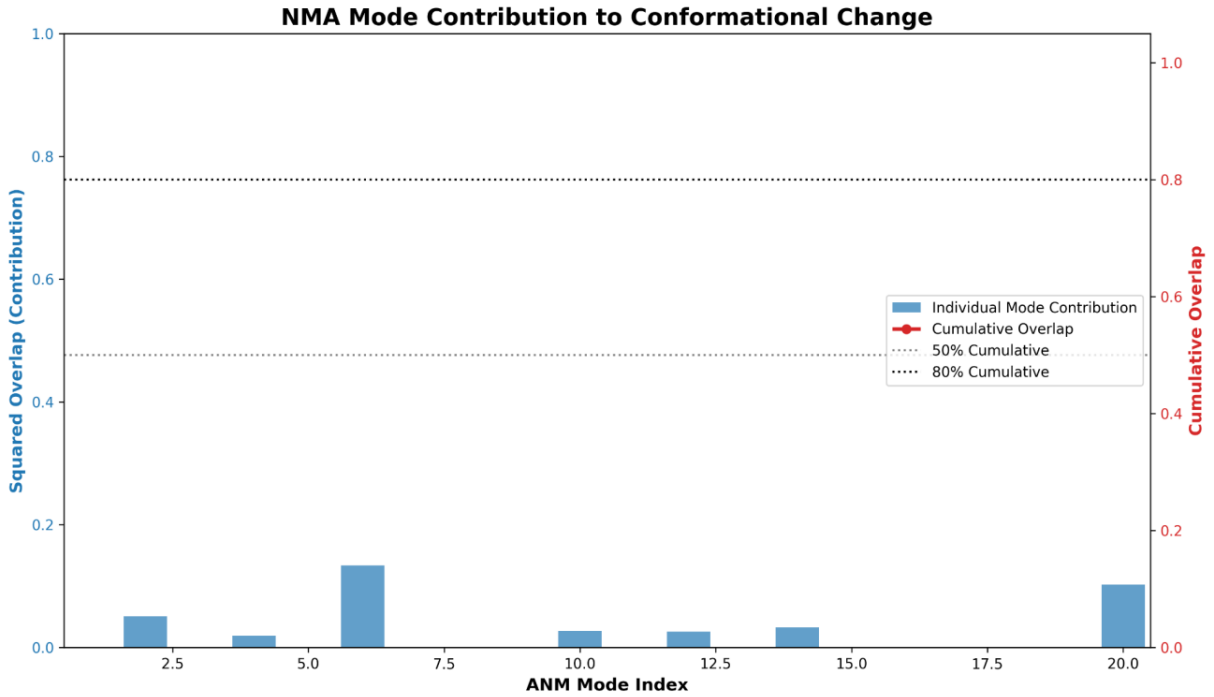

Figure 14: Individual Anm Mode Contributions to Ace2 Conformational Deformation Upon Spike Binding. Squared Overlap Between the Deformation Vector (Apo→Complex Transition) And Individual Anm Modes (1–20) Of Apo Ace2. Blue Bars Represent Individual Mode Contributions (Squared Overlap Values). Horizontal Dashed Lines Indicate 50 and 80% Reference Thresholds for Cumulative Overlap. No Single Mode Dominates the Transition; Modes 6 And 20 Contribute Most (~10–13% Each), With Secondary Contributions from Modes 2, 10, 12, And 14 (~2–3% Each), Indicating A Distributed, Multi-Mode Deformation Mechanism Characteristic 0f Ensemble-Driven Conformational Remodeling Rather Than Single-Mode Transitions.

The deformation analysis, in conjunction with the overlap and ΔRMSF results, indicates that ACE2 functions as a mechanically recoupable scaffold upon Spike engagement. Instead of a lock-and-key rigidification, Spike binding drives a reallocation of ANM modes that yields a transition-ready architecture assembled from multiple collective motions, in line with allostery-driven remodeling reported in earlier ACE2–Spike dynamical studies [65-70].

3.2.4. Contact Stability

The residue–residue contact map between ACE2 (Chain A) and the Spike RBD (Chain E) was compared with the interaction profile reported in PDB sum for the same complex (PDB entry 6M0J) in order to evaluate the dependability of the interface interactions found from the ANM-guided structural analysis [73]. Over an interface area of roughly 825–863 Å^2, PDB sum finds 20 interface residues on Chain A and 17 on Chain E, forming 10 hydrogen bonds, 1 salt bridge, and 101 non-bonded contacts. A 5.0 Å heavy-atom distance cutoff for residue–residue contacts, a 3.5 Å donor–acceptor cutoff for hydrogen bonds, a 4.0 Å O–N cutoff for salt bridges, π–π and cation–π thresholds of 7.0 Å and 6.0 Å, respectively, a 5.0 Å cutoff for hydrophobic interactions, and a 2.5 Å threshold for disulphide bonds were used to calculate the contact mapping [40-44,74,75].

Noncovalent interaction analysis identified eight hydrogen bonds (mean distance 2.99 Å), one salt bridge (mean distance

2.90 Å), one cation-π interaction, seven hydrophobic contacts, and multiple intramolecular disulfide bonds (mean distance 2.05 Å) (Figure. 15).

The resulting interface profile recovered the same single salt bridge reported in PDB sum and replicated the anticipated clustering of contacting residues on both chains. Geometric cutoff differences and the lack of crystallographic water molecules in the computational workflow caused minor variations in the number of hydrogen bonds, which was similar (8 identified here vs. 10 in PDB sum). According to PDB sum, which reports no inter-chain disulphide linkages for this complex, all disulphide bonds found corresponded only to intramolecular cysteine pairs within ACE2.

When compared to PDB sum's experimentally derived interaction map, the contact stability pattern obtained under these standardized geometric criteria shows close correspondence, suggesting that the interface captured by the structural analysis is accurate and represents the experimentally observed ACE2–Spike binding geometry.

To describe the structural accessibility and physicochemical characteristics of interface-exposed regions, solvent-accessible surface area and residue-level hydrophobicity profiles were computed for both ACE2 (Chain A) and the Spike RBD (Chain E). In ACE2, 395 residues fell below the 10 ´ core threshold, reflecting the compact helical fold, while 25 residues exceeded the 40 ´ surface threshold, indicating structurally accessible regions consistent with the extracellular receptor architecture [28]. The Kyte-Doolittle hydrophobicity profile showed alternating hydrophilic and hydrophobic segments, with buried α-helical segments and structural stabilization regions exhibiting a strong hydrophobic character. The compact β-sheet scaffold was reflected in 130 core residues (SASA < 10) of the Spike RBD, whereas 14 residues (SASA > 40) were mainly at the receptor-binding motif (residues 438–505) [29]. In line with the description of the RBD as a rigid, hydrophobically stabilized binding platform, the hydrophobicity profile revealed strong hydrophobic character in the structural core and primarily hydrophilic character at the receptor-facing surface (Figure 16) [76]. The computational analysis captures functionally relevant surface properties of both the ACE2 receptor and the Spike RBD, as confirmed by the combined SASA-hydrophobicity profiles that match experimentally determined structural features reported in crystallographic and cryo-EM studies [28,29,76].

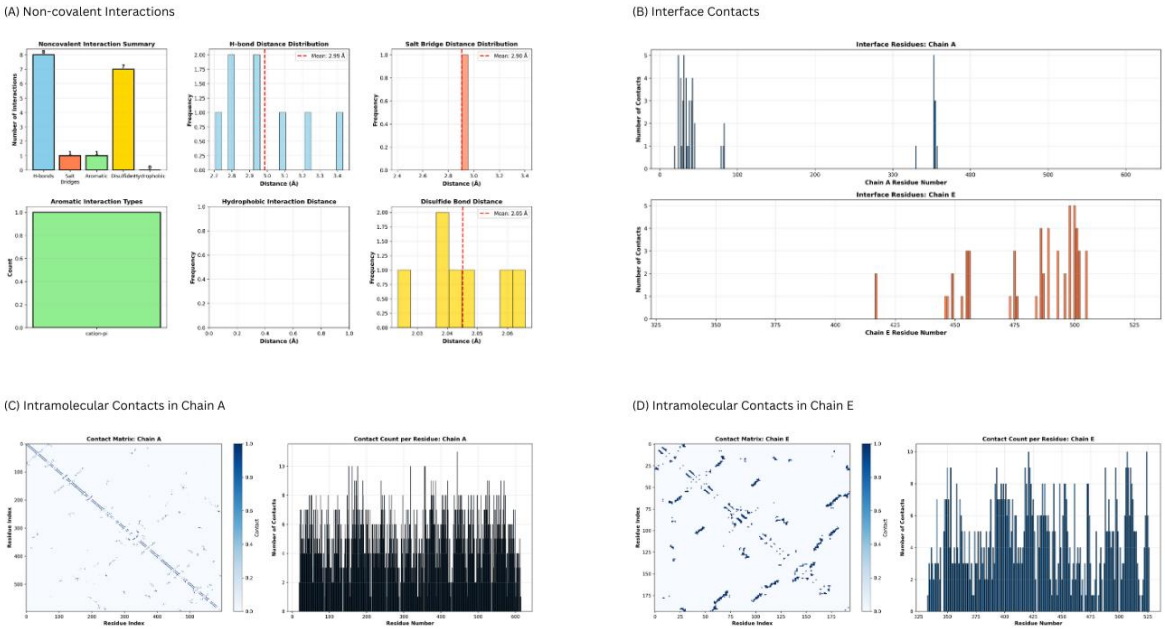

Figure 15: Interface and Intramolecular Contact Analysis. (A) Noncovalent Interaction Summary Between Ace2 And Spike RBD Showing Counts and Distance Distributions for Hydrogen Bonds, Salt Bridges, Aromatic, Disulphide, And Hydrophobic Interactions. (B) Per-Residue Interface Contact Counts for Ace2 (Upper) And Spike RBD (Lower). (C) Intramolecular Contact Matrix and Per-Residue Contact Distribution for ACE2. (D) Intramolecular Contact Matrix and Per-Residue Contact Distribution for Spike RBD.

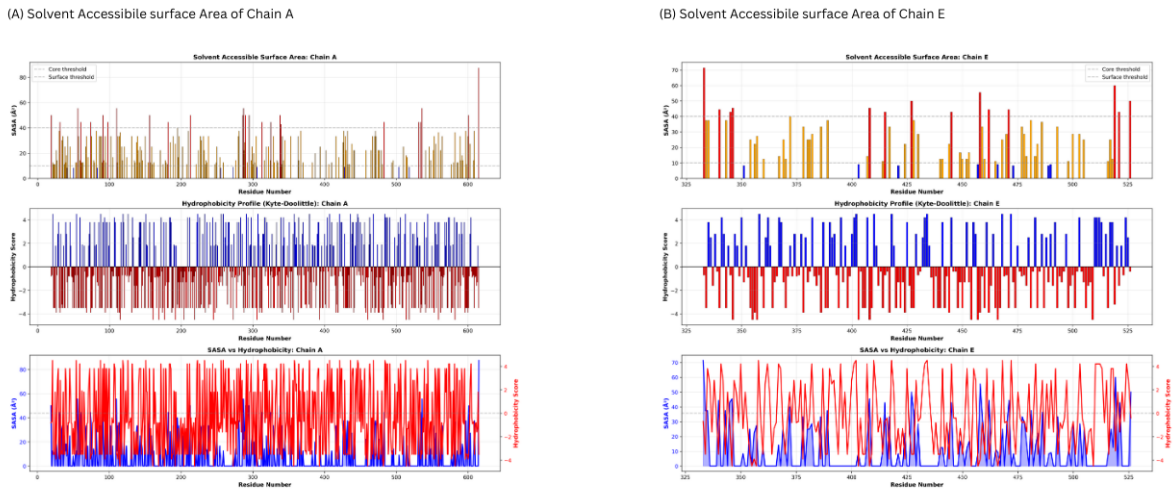

Figure 16: Solvent-Accessible Surface Area and Hydrophobicity Profiles. (A) ACE2 (Chain A) SASA Distribution (top), Kyte-Doolittle Hydrophobicity Scores (middle; blue = hydrophobic, red = hydrophilic), and Combined Sasa-Hydrophobicity Overlay (bottom; blue line = SASA, red line = hydrophobicity). (B) Corresponding Profiles for Spike RBD (Chain E, residues 333–526)

3.2.5. Contact Persistence and Timeline Analysis

A highly selective and structurally conserved interaction network between ACE2 (Chain A) and the Spike RBD (Chain E) was shown by the inter-chain contact timeline across the ANM-generated conformational ensemble. Six of the eight distinct residue pairs that were found in 20 conformers remained in more than 75% of the ensemble, making them stable, high-confidence contacts. The core binding hotspot found in crystallographic and cryo-EM structures is exactly matched by these persistent pairs: ACE2 residues Lys353, Gly354, and Asp355 interacting with RBD residues Asn501, Gly502, and Tyr505 [28,29,76].According to the established function of Lys353 as the primary anchoring residue stabilizing the RBD interface, the Lys353–Asn501 and Lys353–Tyr505 contacts showed 100% persistence [28,76].

Lys353–Gly502 (20%) and Gln24–Ala475 (5%) were two contacts with low persistence. These fleeting pairs are described as auxiliary, non-anchoring contacts that modulate binding strength but do not define it [65]. They correspond to peripheral interactions that only manifest under particular conformational microstates. With only brief interruptions that corresponded to ANM-induced fluctuations, the timeline heatmap verified that the six high-persistence contacts continued to be engaged throughout almost the entire conformational ensemble.

The persistence analysis shows that the ANM-generated ensemble preserves the experimentally established interaction architecture: a rigid central hotspot (Lys353–Gly354–Asp355) surrounded by flexible auxiliary contacts. This pattern is consistent with crystallographic, cryo-EM, and MD-derived interaction maps describing the ACE2 interface as a stable anchoring triad with a flexible periphery (Figure 17 [28,29,65,76]. These results confirm that the conformational sampling captures the key binding determinants of the ACE2–Spike interaction.

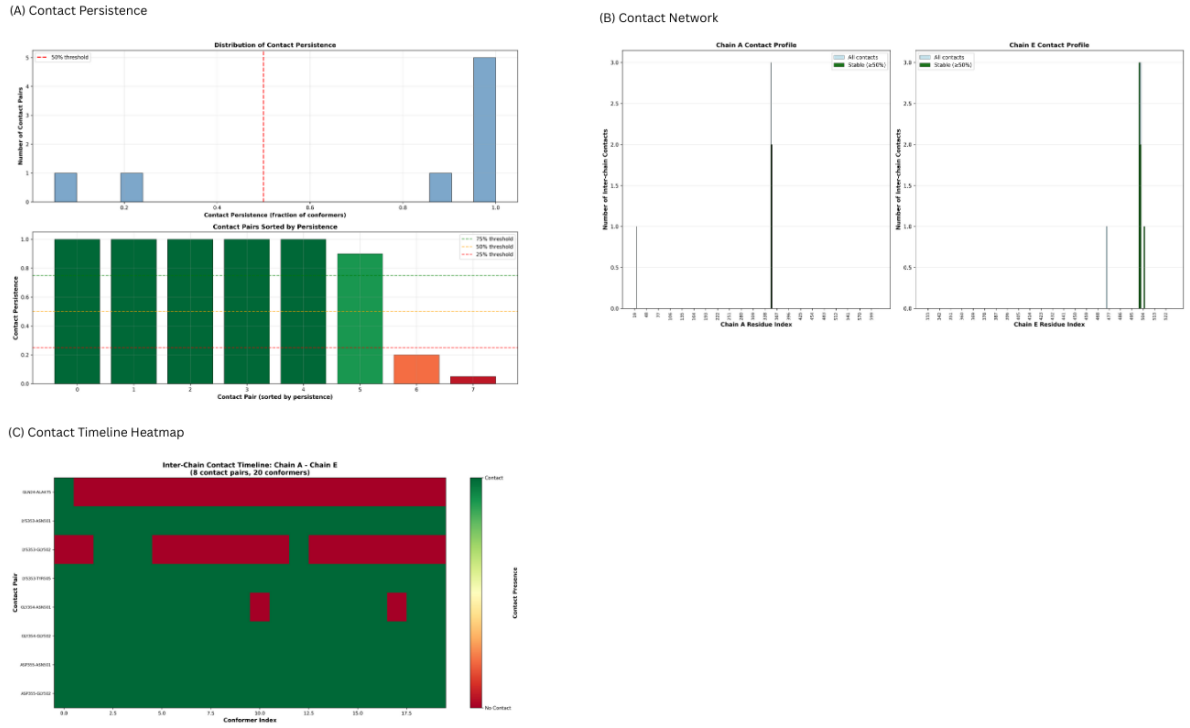

Figure 17: Inter-Chain Contact Persistence Across the Anm Ensemble. (A) Distribution of contact persistence (upper) and individual contact pairs sorted by stability (lower; green = stable ≥50%, orange = intermediate, red = transient <25%). (B) Per-residue contact profiles for ACE2 (left) and Spike RBD (right). (C) Inter-chain contact timeline heatmap tracking eight residue pairs across 20 conformers: LYS353-ASN501, LYS353-TYR505, LYS353-GLY502, GLY354-ASN501, GLY354-GLY502, ASP355-ASN501, ASP355-GLY502, and GLN24-ALA475 (green = contact present, red = absent). The heatmap reveals three high-persistence contacts (LYS353-ASN501, LYS353-TYR505, GLY354-GLY502) with >75% stability across the ensemble, one low-persistence contact (GLN24-ALA475, 5%), and others with intermediate persistence patterns

3.3. Validation Summary

DynaMune reliably replicated known mechanistic signatures and structural determinants of protein dynamics in both benchmark systems. The platform fully aligned with decades of ENM/NMA and MD literature for adenylate kinase, accurately recovering the transition-ready topology of the open state, the experimentally supported hinge and cracking regions, the restricted fluctuation regime of the closed state, and the canonical CORE–LID–NMP domain transitions. DynaMune found the experimentally verified interaction triad, the known Lys353-centered hotspot, and the distinctive redistribution of internal motion modes that takes place upon Spike engagement in the ACE2–Spike system. Additionally, the platform recorded the persistent interfacial contact network and multi-mode deformation mechanism seen in cryo-EM and MD investigations. All of these findings show that DynaMune effectively resolves both protein–protein interface remodeling and intra-protein allosteric transitions. The platform offers a validated, ensemble-based framework for mechanistic interpretation across various biological systems, as demonstrated by the agreement with published structural, dynamical, and energetic benchmarks.

4. Discussion

4.1. Mechanistic Consistency and Benchmark Validation

The results obtained across both validation systems demonstrate that DynaMune reproduces established mechanistic signatures of protein motion with a high degree of fidelity. For adenylate kinase, the platform captured the well-characterised CORE–LID–NMP displacement pathway, the restricted fluctuation regime of the closed state, and the hinge-localised cracking behavior that facilitates the transition to the open conformation. These findings align with decades of ENM, NMA, and MD literature describing the energetic and mechanical basis of ADK's functional transition. The consistency between DynaMune's ANM-derived modes, domain decomposition, hinge localisation, and deformation vectors confirms that the platform accurately resolves both global conformational shifts and localised mechanical rearrangements governing allosteric transitions.

In the ACE2–Spike system, DynaMune similarly reconstructed the experimentally defined interaction architecture, including the Lys353-centred hotspot, the surface-exposed RBM residues, and the asymmetric distribution of flexibility across the peptidase and neck domains. The low diagonal mode overlap, multi-mode deformation requirements, and redistribution of RMSF patterns all reflect previously reported evidence that Spike engagement reorganises

ACE2's internal motion subspace rather than inducing rigidification. The identification of persistent interfacial contacts and the recovery of the canonical triad (Lys353–Gly354–Asp355) further validate the accuracy of the contact mapping and interface stability modules. Together, these results demonstrate that DynaMune reliably resolves both intra-protein and protein–protein dynamic signatures across systems with distinct mechanistic constraints.

4.2. Advantages of an Integrated ENM/NMA-Based Framework

A key contribution of DynaMune is its ability to unify otherwise fragmented analytical steps into an automated, parameter-aware workflow. Existing NMA/ENM tools typically require manual scripting, heterogeneous parameter selection, and reliance on multiple programs to perform even routine comparative tasks [23] [26]. DynaMune eliminates these discontinuities by offering standardized execution pipelines for mode analysis, PCA, conformer generation, PRS scanning, hinge/domain decomposition, pocket dynamics, deformation mapping, and interface persistence evaluation. This consolidation reduces user-dependent variability, ensures reproducibility, and makes ensemble-based mechanistic interpretation feasible without specialised computational expertise.

Importantly, DynaMune integrates an apo–complex comparison framework that is absent from other tools. Direct mapping of deformation vectors, dynamic subspace overlaps, and contact persistence diagrams allows mechanistic evaluation of conformational shifts, ligand-induced remodeling, and interface stabilization. These capabilities extend ENM/NMA utility beyond traditional fluctuation analysis and provide biologically interpretable insights consistent with what is typically only achievable using long-timescale MD simulations.

To compare DynaMune with available ENM/NMA tools, a feature-level comparison was performed against three widely used platforms- iMODS, WEBnm@ and Bio3D. These tools provide valuable functionality for individual components of dynamics analysis, but they lack integrated support for ensemble generation, comparison between apo and complex, contact persistence evaluation and standardized parameter handling. Table 2 summarises the distinctions across the core analytical capabilities and highlights the analytical steps that DynaMune brings together within a unified workflow.

Feature Category	iMODS	WEBnm@	Bio3D (R package)	DynaMune
Platform Type	Web server	Web server	R package	Python CLI + Web GUI
Access Mode	Browser only	Browser only	Requires R scripting	Web interface; scripting optional
Single-Protein NMA	Supported	Supported	Supported	Supported
ANM Implementation	Internal-coordinate ENM	Cartesian ENM	Multiple models	Cartesian ANM (ProDy)
GNM Implementation	Basic GNM	Basic GNM	Supported	Supported
Batch Processing	Not available	Not available	Via scripting loops	Supported via CLI
Comparative NMA	Manual only	Basic tools	Supported (NMA/ ENMA)	Automated
Apo–Complex Comparison	Not available	Not available	Requires scripting	Automated
Contact Analysis	Not available	Not available	Limited utilities	Interface + intramolecular contacts
Domain Detection	Not available	Not available	Basic geometric	Hierarchical decomposition
Hinge Identification	Not available	Not available	Not explicit	Stiffness-based mapping
Contact Persistence	Not available	Not available	Not implemented	Ensemble-level persistence
Pocket Dynamics	Not available	Not available	Not available	Supported
PRS / Allostery	Not available	Not available	Not included	PRS allosteric analysis
Deformation Analysis	Not available	Not available	Manual scripting	ANM-mode projection

Plot Generation	PNG exports	PNG exports	R plots	Publication-ready graphics
PyMOL Integration	Limited	Not supported	Basic	Auto-generated scripts
Data Export	Not available	Limited	CSV/text	CSV/TXT/PyMOL/ PDB
Parameter Control	Limited	Limited	Requires scripting	Unified parameter defaults
Open Source	Free	Free	Open source	Open source
Immunoinformatic Module	Not included	Not included	Not included	Optional, Dynamics-assisted screening
Computational Core	Internal	Internal	Internal/external	ProDy

Table 2: Comparative feature analysis of DynaMune against existing ENM/NMA frameworks.

4.3. Biological and Computational Implications

The benchmarking results highlight the value of ensemble-based ENM/NMA analyses for mechanistic interpretation across diverse biological contexts. In ADK, the recovery of hinge-controlled coupling between functional domains demonstrates that low-frequency modes alone can summarize complex conformational pathways. In ACE2–Spike, the detection of multi-mode deformation captures the non-rigid, remodeled nature of the interface—consistent with established findings that SARS-CoV-2 engagement alters ACE2 microstates and redistributes internal plasticity.

These observations emphasise that ENM-derived ensembles, when systematically sampled and integrated through DynaMune's comparative modules, can approximate many of the mechanistic insights typically derived from MD, but at a fraction of the computational cost and with clear analytical interpretability [1]. For systems where MD is impractical or where functional states must be rapidly screened, DynaMune provides a scalable alternative capable of identifying regulatory hotspots, persistent interfaces, hinge residues, and transition-favouring deformation pathways [16].

4.4. Future Extensions

Expanding comparative capabilities and improving mechanistic resolution will be the top priorities for future DynaMune developments. The introduction of multi-state comparative dynamics, which allows analysis of several conformational states, mutation series, or ligand variants within a single computational framework, is a primary goal [77]. Further advancements will include two-partner mechanical inference models that extend PRS to quantify how perturbations in one chain reshape the stability and persistence of interfacial contacts in the other, as well as adaptive coarse-graining strategies to handle large and multi-domain assemblies without user-defined simplifications. Mode clustering to find coherent mechanistic mode families and automated detection of cryptic or transition pockets by combining deformation vectors, pocket fluctuations, and contact rearrangements are among the planned analytical additions [78]. When combined, these improvements will increase DynaMune's ability to facilitate comparative, predictive, and design-focused applications in a variety of structural systems.

4.5. Limitations

DynaMune offers a unified framework for ENM/NMA-based dynamics analysis, but elastic network models still have a number of methodological limitations. Because ENMs use harmonic potentials and coarse-grained representations to approximate conformational fluctuations, they are unable to capture anharmonic behavior, side-chain rearrangements, solvent effects, or time-dependent kinetic processes that MD simulations can. The conformers that result are structurally plausible but not thermodynamically sampled states because ensemble generation is driven by projections along low-frequency modes. The lack of explicit environmental context limits both interface evaluations and pocket fluctuations. These factors define the parameters within which ENM-based predictions should be assessed and experimentally contextualised, but they do not diminish DynaMune's usefulness for comparative or mechanistic interpretation.

5. Conclusion

Under a completely standardized parameter architecture, DynaMune offers a unified, ensemble-based framework for protein dynamics analysis utilising ENM and NMA techniques. The platform removes the fragmentation and user-dependent variability present in previous methods by combining mode evaluation, conformer generation, deformation mapping, PRS behavior, domain and hinge decomposition, pocket dynamics, and interface persistence analysis into a single workflow. The validation studies show that DynaMune accurately captures both fine-grained interface remodeling, such as the ACE2–SARS-CoV-2 Spike complex, and large-scale allosteric transitions, such as adenylate kinase. The platform replicated known mechanistic signatures in each instance, such as multi-mode deformation patterns associated with ligand-induced reorganization, hinge-centered cracking behavior, canonical functional modes, and hotspot-driven interface stability.

These results demonstrate that ensemble-driven ENM/NMA analysis can consistently recover experimentally

supported dynamic behavior without the computational expense of long-timescale simulations when applied through a coherent computational pipeline. Therefore, DynaMune offers a useful, repeatable, and scalable tool for mechanistic interpretation in a variety of structural biology applications, such as protein–protein recognition and intra-protein allostery. DynaMune facilitates more accessible and standardized dynamics-aware annotation for structural biology, computational biophysics, and protein engineering by formalizing comparative dynamics into a consistent analytical framework.

References

1. Bahar, I., Lezon, T. R., Yang, L. W., & Eyal, E. (2010). Global dynamics of proteins: bridging between structure and function. Annual review of biophysics, 39, 23-42.
2. Henzler-Wildman, K., & Kern, D. (2007). Dynamic personalities of proteins. Nature, 450(7172), 964-972.
3. Kern, D., & Zuiderweg, E. R. (2003). The role of dynamics in allosteric regulation. Current opinion in structural biology, 13(6), 748-757.
4. Boehr, D. D., Nussinov, R., & Wright, P. E. (2009). The role of dynamic conformational ensembles in biomolecular recognition. Nature chemical biology, 5(11), 789-796.
5. Csermely, P., Palotai, R., & Nussinov, R. (2010). Induced fit, conformational selection and independent dynamic segments: an extended view of binding events. Trends in biochemical sciences, 35(10), 539-546.
6. Kühlbrandt, W. (2014). Cryo-EM enters a new era. elife, 3, e03678.
7. Scheres, S. H. (2016). Processing of structurally heterogeneous cryo-EM data in RELION. Methods in enzymology, 579, 125-157.
8. Senior, A. W., Evans, R., Jumper, J., Kirkpatrick, J., Sifre, L., Green, T., ... & Hassabis, D. (2020). Improved protein structure prediction using potentials from deep learning. Nature, 577(7792), 706-710.
9. Abramson, J., Adler, J., Dunger, J., Evans, R., Green, T., Pritzel, A., ... & Jumper, J. M. (2024). Accurate structure prediction of biomolecular interactions with AlphaFold 3. Nature, 630(8016), 493-500.
10. Tsai, C. J., Kumar, S., Ma, B., & Nussinov, R. (1999). Folding funnels, binding funnels, and protein function. Protein Science, 8(6), 1181-1190.
11. Caballero-Manrique, E., Bray, J. K., Deutschman, W. A., Dahlquist, F. W., & Guenza, M. G. (2007). A theory of protein dynamics to predict NMR relaxation. Biophysical Journal, 93(12), 4128-4140.
12. Kuzmanic, A., & Zagrovic, B. (2010). Determination of ensemble-average pairwise root mean-square deviation from experimental B-factors. Biophysical journal, 98(5), 861-871.
13. Varadi, M., Bertoni, D., Magana, P., Paramval, U., Pidruchna, I., Radhakrishnan, M., ... & Velankar, S. (2024). AlphaFold Protein Structure Database in 2024: providing structure coverage for over 214 million protein sequences. Nucleic acids research, 52(D1), D368-D375.
14. Tirion, M. M. (1996). Large amplitude elastic motions in proteins from a single-parameter, atomic analysis. Physical review letters, 77(9), 1905.
15. Bahar, I., Atilgan, A. R., & Erman, B. (1997). Direct evaluation of thermal fluctuations in proteins using a single-parameter harmonic potential. Folding and Design, 2(3), 173-181.
16. Doruker, P., Atilgan, A. R., & Bahar, I. (2000). Dynamics of proteins predicted by molecular dynamics simulations and analytical approaches: Application to α-amylase inhibitor. Proteins: Structure, Function, and Bioinformatics, 40(3), 512-524.
17. Müller, C. W., & Schulz, G. E. (1992). Structure of the complex between adenylate kinase from Escherichia coli and the inhibitor Ap5A refined at 1.9 Å resolution: A model for a catalytic transition state. Journal of molecular biology, 224(1), 159-177.
18. Bock, L. V., Gabrielli, S., Kolář, M. H., & Grubmüller, H. (2023). Simulation of complex biomolecular systems: the ribosome challenge. Annual Review of Biophysics, 52(1), 361-390.
19. Cirauqui Diaz, N., Frezza, E., & Martin, J. (2021). Using normal mode analysis on protein structural models. How far can we go on our predictions?. Proteins: Structure, Function, and Bioinformatics, 89(5), 531-543.
20. Rodrigues, C. H., Pires, D. E., & Ascher, D. B. (2018). DynaMut: predicting the impact of mutations on protein conformation, flexibility and stability. Nucleic acids research, 46(W1), W350-W355.
21. Cilia, E., Pancsa, R., Tompa, P., Lenaerts, T., & Vranken, W. F. (2014). The DynaMine webserver: predicting protein dynamics from sequence. Nucleic acids research, 42(W1), W264-W270.
22. Fuglebakk, E., Echave, J., & Reuter, N. (2012). Measuring and comparing structural fluctuation patterns in large protein datasets. Bioinformatics, 28(19), 2431-2440.
23. Bakan, A., Meireles, L. M., & Bahar, I. (2011). ProDy: protein dynamics inferred from theory and experiments. Bioinformatics, 27(11), 1575-1577.
24. López-Blanco, J. R., Aliaga, J. I., Quintana-Ortí, E. S., & Chacón, P. (2014). iMODS: internal coordinates normal mode analysis server. Nucleic acids research, 42(W1), W271-W276.
25. Hollup, S. M., Salensminde, G., & Reuter, N. (2005). WEBnm@: a web application for normal mode analyses of proteins. BMC bioinformatics, 6(1), 52.
26. Grant, B. J., Skjærven, L., & Yao, X. Q. (2021). The Bio3D packages for structural bioinformatics. Protein Science, 30(1), 20-30.
27. Delarue, M., & Sanejouand, Y. H. (2002). Simplified normal mode analysis of conformational transitions in DNA-dependent polymerases: the elastic network model. Journal of molecular biology, 320(5), 1011-1024.
28. Lan, J., Ge, J., Yu, J., Shan, S., Zhou, H., Fan, S., ... & Wang, X. (2020). Structure of the SARS-CoV-2 spike receptor-binding domain bound to the ACE2 receptor. nature, 581(7807), 215-220.
29. Shang, J., Ye, G., Shi, K., Wan, Y., Luo, C., Aihara, H., ... & Li, F. (2020). Structural basis of receptor recognition by SARS-CoV-2. Nature, 581(7807), 221-224.
30. Wrapp, D., Wang, N., Corbett, K. S., Goldsmith, J. A.,

Hsieh, C. L., Abiona, O., ... & McLellan, J. S. (2020). Cryo-EM structure of the 2019-nCoV spike in the prefusion conformation. Science, 367(6483), 1260-1263.
31. Zhang, S., Li, H., Krieger, J. M., & Bahar, I. (2019). Shared signature dynamics tempered by local fluctuations enables fold adaptability and specificity. Molecular biology and evolution, 36(9), 2053-2068.
32. Bakan, A., & Bahar, I. (2009). The intrinsic dynamics of enzymes plays a dominant role in determining the structural changes induced upon inhibitor binding. Proceedings of the National Academy of Sciences, 106(34), 14349-14354.
33. Haliloglu, T., Bahar, I., & Erman, B. (1997). Gaussian dynamics of folded proteins. Physical review letters, 79(16), 3090.
34. Atilgan, A. R., Akan, P., & Baysal, C. (2004). Small-world communication of residues and significance for protein dynamics. Biophysical journal, 86(1), 85-91.
35. Eyal, E., Lum, G., & Bahar, I. (2015). The anisotropic network model web server at 2015 (ANM 2.0). Bioinformatics, 31(9), 1487-1489.
36. Mitternacht, S., & Berezovsky, I. N. (2011). Binding leverage as a molecular basis for allosteric regulation. PLoS computational biology, 7(9), e1002148.
37. Tama, F., & Sanejouand, Y. H. (2001). Conformational change of proteins arising from normal mode calculations. Protein engineering, 14(1), 1-6.
38. Sethi, A., Eargle, J., Black, A. A., & Luthey-Schulten, Z. (2009). Dynamical networks in tRNA: protein complexes. Proceedings of the National Academy of Sciences, 106(16), 6620-6625.
39. General, I. J., Liu, Y., Blackburn, M. E., Mao, W., Gierasch, L. M., & Bahar, I. (2014). ATPase subdomain IA is a mediator of interdomain allostery in Hsp70 molecular chaperones. PLoS computational biology, 10(5), e1003624.
40. Jeffrey, G. A., & Saenger, W. (2012). Hydrogen bonding in biological structures. Springer Science & Business Media.
41. Donald, J. E., Kulp, D. W., & DeGrado, W. F. (2011). Salt bridges: Geometrically specific, designable interactions. Proteins: Structure, Function, and Bioinformatics, 79(3), 898-915.
42. Donald, J. E., Kulp, D. W., & DeGrado, W. F. (2011). Salt bridges: Geometrically specific, designable interactions. Proteins: Structure, Function, and Bioinformatics, 79(3), 898-915.
43. Salamanca Viloria, J., Allega, M. F., Lambrughi, M., & Papaleo, E. (2017). An optimal distance cutoff for contact-based Protein Structure Networks using side-chain centers of mass. Scientific reports, 7(1), 2838.
44. Thornton, J. M. (1981). Disulphide bridges in globular proteins. Journal of molecular biology, 151(2), 261-287.
45. Shrake, A., & Rupley, J. A. (1973). Environment and exposure to solvent of protein atoms. Lysozyme and insulin. Journal of molecular biology, 79(2), 351-371.
46. Xu, H., & Zhao, Z. (2022). NetBCE: an interpretable deep neural network for accurate prediction of linear B-cell epitopes. Genomics, Proteomics & Bioinformatics, 20(5), 1002-1012.
47. Reynisson, B., Alvarez, B., Paul, S., Peters, B., & Nielsen, M. (2020). NetMHCpan-4.1 and NetMHCIIpan-4.0: improved predictions of MHC antigen presentation by concurrent motif deconvolution and integration of MS MHC eluted ligand data. Nucleic acids research, 48(W1), W449-W454.
48. Gupta, S., Kapoor, P., Chaudhary, K., Gautam, A., Kumar, R., Open Source Drug Discovery Consortium, & Raghava, G. P. (2013). In silico approach for predicting toxicity of peptides and proteins. PloS one, 8(9), e73957.
49. Raghuram, A. (2026). DynaMune: An Integrated Ensemble-Based Framework for Comparative Protein Dynamics Using Elastic Network Models.
50. Cock, P. J., Antao, T., Chang, J. T., Chapman, B. A., Cox, C. J., Dalke, A., ... & De Hoon, M. J. (2009). Biopython: freely available Python tools for computational molecular biology and bioinformatics. Bioinformatics, 25(11), 1422.
51. Lin, Z., Akin, H., Rao, R., Hie, B., Zhu, Z., Lu, W., ... & Rives, A. (2023). Evolutionary-scale prediction of atomic-level protein structure with a language model. Science, 379(6637), 1123-1130.
52. Arora, K., & Brooks III, C. L. (2007). Large-scale allosteric conformational transitions of adenylate kinase appear to involve a population-shift mechanism. Proceedings of the National Academy of Sciences, 104(47), 18496-18501.
53. Müller, C. W., Schlauderer, G. J., Reinstein, J., & Schulz, G. E. (1996). Adenylate kinase motions during catalysis: an energetic counterweight balancing substrate binding. Structure, 4(2), 147-156.
54. Schrodinger, L. L. C. (2015). The PyMOL molecular graphics system. Version, 1, 8.
55. Atilgan, A. R., Durell, S. R., Jernigan, R. L., Demirel, M. C., Keskin, O., & Bahar, I. (2001). Anisotropy of fluctuation dynamics of proteins with an elastic network model. Biophysical journal, 80(1), 505-515.
56. Whitford, P. C., Miyashita, O., Levy, Y., & Onuchic, J. N. (2007). Conformational transitions of adenylate kinase: switching by cracking. Journal of molecular biology, 366(5), 1661-1671.
57. Schulz, G. E., Müller, C. W., & Diederichs, K. (1990). Induced-fit movements in adenylate kinases. Journal of molecular biology, 213(4), 627-630.
58. Matsunaga, Y., Fujisaki, H., Terada, T., Furuta, T., Moritsugu, K., & Kidera, A. (2012). Minimum free energy path of ligand-induced transition in adenylate kinase. PLoS computational biology, 8(6), e1002555.
59. Eyal, E., Yang, L. W., & Bahar, I. (2006). Anisotropic network model: systematic evaluation and a new web interface. Bioinformatics, 22(21), 2619-2627.
60. Raghuram, A. (2026). DynaMune: An Integrated Ensemble-Based Framework for Comparative Protein Dynamics Using Elastic Network Models.
61. Towler, P., Staker, B., Prasad, S. G., Menon, S., Tang, J., Parsons, T., ... & Pantoliano, M. W. (2004). ACE2 X-ray structures reveal a large hinge-bending motion important for inhibitor binding and catalysis. Journal of Biological Chemistry, 279(17), 17996-18007.

62. Yan, R., Zhang, Y., Li, Y., Xia, L., Guo, Y., & Zhou, Q. (2020). Structural basis for the recognition of SARS-CoV-2 by full-length human ACE2. Science, 367(6485), 1444-1448.
63. Uyar, A., & Dickson, A. (2021). Perturbation of ACE2 structural ensembles by SARS-CoV-2 spike protein binding. Journal of Chemical Theory and Computation, 17(9), 5896-5906.
64. Ali, A., & Vijayan, R. (2020). Dynamics of the ACE2–SARS-CoV-2/SARS-CoV spike protein interface reveal unique mechanisms. Scientific reports, 10(1), 14214.
65. Barros, E. P., Casalino, L., Gaieb, Z., Dommer, A. C., Wang, Y., Fallon, L., ... & Amaro, R. E. (2021). The flexibility of ACE2 in the context of SARS-CoV-2 infection. Biophysical journal, 120(6), 1072-1084.
66. Xu, C., Wang, Y., Liu, C., Zhang, C., Han, W., Hong, X., ... & Cong, Y. (2021). Conformational dynamics of SARS-CoV-2 trimeric spike glycoprotein in complex with receptor ACE2 revealed by cryo-EM. Science advances, 7(1), eabe5575.
67. Díaz-Salinas, M. A., Li, Q., Ejemel, M., Yurkovetskiy, L., Luban, J., Shen, K., ... & Munro, J. B. (2022). Conformational dynamics and allosteric modulation of the SARS-CoV-2 spike. Elife, 11, e75433.
68. Teruel, N., Mailhot, O., & Najmanovich, R. J. (2021). Modelling conformational state dynamics and its role on infection for SARS-CoV-2 Spike protein variants. PLoS computational biology, 17(8), e1009286.
69. Gupta, G., & Verkhivker, G. (2024). Exploring binding pockets in the conformational states of the SARS-CoV-2 spike trimers for the screening of allosteric inhibitors using molecular simulations and ensemble-based ligand docking. International Journal of Molecular Sciences, 25(9), 4955.
70. Xiao, S., Alshahrani, M., Gupta, G., Tao, P., & Verkhivker, G. (2023). Markov State Models and Perturbation-Based Approaches Reveal Distinct Dynamic Signatures and Hidden Allosteric Pockets in the Emerging SARS-Cov-2 Spike Omicron Variant Complexes with the Host Receptor: The Interplay of Dynamics and Convergent Evolution Modulates Allostery and Functional Mechanisms. Journal of chemical information and modeling, 63(16), 5272-5296.
71. Yánez Arcos, D. L., & Thirumuruganandham, S. P. (2023). Structural and pKa Estimation of the Amphipathic HR1 in SARS-CoV-2: Insights from Constant pH MD, Linear vs. Nonlinear Normal Mode Analysis. International Journal of Molecular Sciences, 24(22), 16190.
72. Wang, J., Shao, Q., Xu, Z., Liu, Y., Yang, Z., Cossins, B. P., ... & Zhu, W. (2014). Exploring transition pathway and free-energy profile of large-scale protein conformational change by combining normal mode analysis and umbrella sampling molecular dynamics. The Journal of Physical Chemistry B, 118(1), 134-143.
73. Laskowski, R. A., Jabłońska, J., Pravda, L., Vařeková, R. S., & Thornton, J. M. (2018). PDBsum: Structural summaries of PDB entries. Protein science, 27(1), 129-134.
74. Khazanov, N. A., & Carlson, H. A. (2013). Exploring the composition of protein-ligand binding sites on a large scale. PLoS computational biology, 9(11), e1003321.
75. Sivasakthi, V., Anitha, P., Kumar, K. M., Bag, S., Senthilvel, P., Lavanya, P., ... & Ramaiah, S. (2013). Aromatic-aromatic interactions: analysis of π-π interactions in interleukins and TNF proteins. Bioinformation, 9(8), 432.
76. Wang, Q., Zhang, Y., Wu, L., Niu, S., Song, C., Zhang, Z., ... & Qi, J. (2020). Structural and functional basis of SARS-CoV-2 entry by using human ACE2. Cell, 181(4), 894-904.
77. Fuglebakk, E., Tiwari, S. P., & Reuter, N. (2015). Comparing the intrinsic dynamics of multiple protein structures using elastic network models. Biochimica et Biophysica Acta (BBA)-General Subjects, 1850(5), 911-922.
78. Cimermancic, P., Weinkam, P., Rettenmaier, T. J., Bichmann, L., Keedy, D. A., Woldeyes, R. A., ... & Sali, A. (2016). CryptoSite: expanding the druggable proteome by characterization and prediction of cryptic binding sites. Journal of molecular biology, 428(4), 709-719.